AGU PUBLICATIONS

Journal of Advances in Modeling Earth Systems

RESEARCH ARTICLE

10.1002/2017MS001177

A New Coupled Ocean-Waves-Atmosphere Model Designed for Tropical Storm Studies: Example of Tropical Cyclone Bejisa (2013–2014) in the South-West Indian Ocean

J. Pianezze[1], C. Barthe[1], S. Bielli[1], P. Tulet[1], S. Jullien[2], G. Cambon[2], O. Bousquet[1], M. Claeys[1], and E. Cordier[3]

[1]Laboratoire de l'Atmosphère et des Cyclones (LACy), Université La Réunion, CNRS, Météo-France, Saint-Denis, France, [2]Ifremer, Laboratoire d'Océanographie Physique et Spatiale (LOPS), Université Brest, CNRS, IRD, IUEM, Plouzané, France, [3]Observatoire des Sciences de l'Univers de La Réunion (OSU-R), Université La Réunion, CNRS, Saint-Denis, France

Abstract Ocean-Waves-Atmosphere (OWA) exchanges are not well represented in current Numerical Weather Prediction (NWP) systems, which can lead to large uncertainties in tropical cyclone track and intensity forecasts. In order to explore and better understand the impact of OWA interactions on tropical cyclone modeling, a fully coupled OWA system based on the atmospheric model Meso-NH, the oceanic model CROCO, and the wave model WW3 and called MSWC was designed and applied to the case of tropical cyclone Bejisa (2013–2014). The fully coupled OWA simulation shows good agreement with the literature and available observations. In particular, simulated significant wave height is within 30 cm of measurements made with buoys and altimeters. Short-term ($<$ 2 days) sensitivity experiments used to highlight the effect of oceanic waves coupling show limited impact on the track, the intensity evolution, and the turbulent surface fluxes of the tropical cyclone. However, it is also shown that using a fully coupled OWA system is essential to obtain consistent sea salt emissions. Spatial and temporal coherence of the sea state with the 10 m wind speed are necessary to produce sea salt aerosol emissions in the right place (in the eyewall of the tropical cyclone) and with the right size distribution, which is critical for cloud microphysics.

Key Points:
- A new coupled Ocean-Waves-Atmosphere system (MSWC) is presented in this paper
- MSWC successfully simulates air-sea processes under a tropical cyclone at kilometer resolution
- MSWC shows the importance of using a fully coupled system to have consistent sea salt aerosol fluxes and concentration

Correspondence to:
J. Pianezze,
joris.pianezze@univ-reunion.fr

Citation:
Pianezze, J., Barthe, C., Bielli, S., Tulet, P., Jullien, S., Cambon, G., et al. (2018). A new coupled ocean-waves-atmosphere model designed for tropical storm studies: Example of tropical cyclone Bejisa (2013–2014) in the South-West Indian Ocean. *Journal of Advances in Modeling Earth Systems*, *10*, 801–825. https://doi.org/10.1002/2017MS001177

Received 21 SEP 2017
Accepted 25 FEB 2018
Accepted article online 1 MAR 2018
Published online 23 MAR 2018

1. Introduction

Tropical cyclones (TC) are among the most devastating meteorological phenomena on Earth. They can be associated with precipitation, wind gusts, storm surges, flooding, and landslides as well as oceanic waves which can cause significant human and economic losses. Despite the considerable progress made over recent decades, intensity and, to some extent, trajectory forecasts still suffer from serious deficiencies. A possible way to improve TC forecasts is to take Ocean-Waves-Atmosphere (OWA) exchanges fully into account to better represent interactions between a TC and its environment.

Many recent studies have focused on the contribution of OWA coupling to tropical cyclone structure (e.g., Bao et al., 2000; Chen et al., 2007; Doyle, 2002; Liu et al., 2011; Warner et al., 2010; Zambon et al., 2014; Zhao et al., 2017). It has been shown that coupling the atmosphere with a 3-D oceanic model is essential to improve the accuracy of tropical cyclone intensity forecasts (Bender & Ginis, 2000). In particular, sea surface cooling under TC reduces the enthalpy fluxes and humidity convergence at the cyclone scale (Jullien et al., 2014; Smith et al., 2009), and so the tropical cyclone intensity growth. This cooling can be attributed to the extraction of heat by the TC (Emanuel, 1986; Holland, 1997; Rotunno & Emanuel, 1987), to strong upwelling and/or to asymmetric mixing provided by the oceanic momentum (e.g., Jullien et al., 2012; Price, 1981; Shay et al., 1989). It can also have an opposite effect. For example, as demonstrated by Lee and Chen (2014), by creating a stable boundary layer behind the cyclone, cooling can suppress convection in rainbands and enhance the transport of air with high energy into the inner core, thus, counterbalancing the expected loss of intensity.

In these studies, it has also been shown that oceanic waves play an important role in tropical cyclone intensity forecasts. As waves represent the dynamical interface of the ocean and the atmosphere, they are involved in the TC life cycle and air-sea exchanges. Oceanic waves drive the atmospheric turbulent fluxes as they modify the wind stress (e.g., Doyle, 2002; Kudryavtsev & Makin, 2007; Liu et al., 2011; Moon et al., 2007;

Wada et al., 2014). For example, Lee and Chen (2012) have shown that the wind-wave coupling deepens the inflow layer, thus increasing the TC intensity. It has also been shown that nonbreaking waves enhance the vertical mixing of the upper ocean (Breivik et al., 2015), which, in return, could modify the sea surface temperature cooling and therefore the tropical cyclone intensity (Aijaz et al., 2017).

Oceanic waves also play an important role through the emission of sea spray. Most studies about sea spray in tropical cyclones have focused on their impact on the ocean-atmosphere fluxes (Andreas & Emanuel, 2001; Bao et al., 2000; Fairall et al., 1994; Wang et al., 2001). One of the main roles of sea spray at high wind speed is to redistribute momentum in the near-surface layer, acting to slow down the near-surface wind speed (Andreas, 2004). This mechanism could be correlated with the saturation of the observed drag coefficient (Potter et al., 2015; Powell et al., 2003). Sea spray also releases water vapor by evaporation and loses sensible heat to the atmosphere, thus modifying the enthalpy fluxes (Richter & Stern, 2014; Wang et al., 2001). Recently, using a fully coupled Ocean-Waves-Atmosphere model, Zhao et al. (2017) focused on the effect of sea spray evaporation and found that sea spray led to an increase of typhoon intensity by enhancing the air-sea fluxes.

In addition, sea spray evaporates into sea salt aerosols which are one of the main sources of cloud condensation nuclei (CCN) in the marine environment (e.g., de Leeuw et al., 2011; Rosenfeld et al., 2014) over which tropical cyclones develop and evolve. Thus, such aerosols can also influence the tropical cyclone structure and intensity through cloud formation, lifetime, and precipitation (Fan et al., 2016; Herbener et al., 2014; Rosenfeld et al., 2012), and references therein). Recent findings also suggest that they could be a source of ice nucleating particles (DeMott et al., 2016; McCluskey et al., 2017; Wang et al., 2017; Wilson et al., 2015). Thus, a key point lies in the representation of their emission in numerical models. A review of sea salt aerosol source functions can be found in Grythe et al. (2014). The first parameterizations were mainly based on the 10 m wind speed (de Leeuw et al., 2011; Jaeglé et al., 2011; Monahan et al., 1986, among others). Recently, the sea surface temperature (Jaeglé et al., 2011), the sea surface salinity (Sofiev et al., 2011), and the sea state (Ovadnevaite et al., 2014) have also been taken into account. With the growing complexity of these parameterizations, it is necessary to use a consistent coupled system taking the interactions between the ocean, the waves, and the atmosphere into account online.

It is also essential to use a high-resolution ($<$ 5 km resolution) coupled system to explicitly represent deep convection which results in a better simulated structure of the tropical cyclone (Fierro et al., 2009; Gentry & Lackmann, 2010; Jin et al., 2014). Few OWA coupling studies using this grid resolution have been identified (Doyle et al., 2014; Jin et al., 2014; Lee & Chen, 2012).

The objective of this paper is twofold: (1) to present a new ocean-waves-atmosphere coupled system for high-resolution tropical cyclone studies, and (2) to show the importance of such a system in describing air-sea fluxes (momentum, heat, and aerosol) in tropical cyclones. This study focuses on the tropical cyclone Bejisa that developed in the south-west Indian Ocean and passed close to La Réunion in January 2014. Section 2 presents the evolution of Bejisa. The modeling strategy is described in section 3. Section 4 presents a description of the fully coupled ocean-waves-atmosphere simulation. Sensitivity of the tropical cyclone structure to oceanic waves coupling is presented in section 5, while the impact of oceanic waves on sea salt aerosols fluxes and concentration is shown in section 6. Finally, the conclusions are given in section 7.

2. Tropical Cyclone Bejisa (2014): An Overview

Bejisa was the fourth tropical storm of the 2013–2014 cyclone season in the south-west Indian Ocean. This tropical cyclone affected the islands of La Réunion and Mauritius in January 2014 (Figures 1 and 2). Since this basin is under the responsibility of the Regional Specialized Meteorological Center (RSMC) of La Réunion, the classification of RSMC La Réunion is used in this study. The intensity of storms is divided into four categories: Moderate Tropical Storm (MTS: $17 < v_{max} < 24$ m s^{-1}), Strong Tropical Storm (STS: $25 < v_{max} < 32$ m s^{-1}), Tropical Cyclone (TC: $33 < v_{max} < 43$ m s^{-1}), and Intense Tropical Cyclone (ITC: $v_{max} > 44$ m s^{-1}), where v_{max} is the 10 min averaged maximum wind speed.

On 27 December 2013, a low-pressure area developed north-east of Madagascar in the vicinity of the Farquhar Islands, a relatively unusual region for cyclogenesis. The convection started to become organized around this low-pressure area. A decrease in the east-southeast vertical wind shear and the favorable

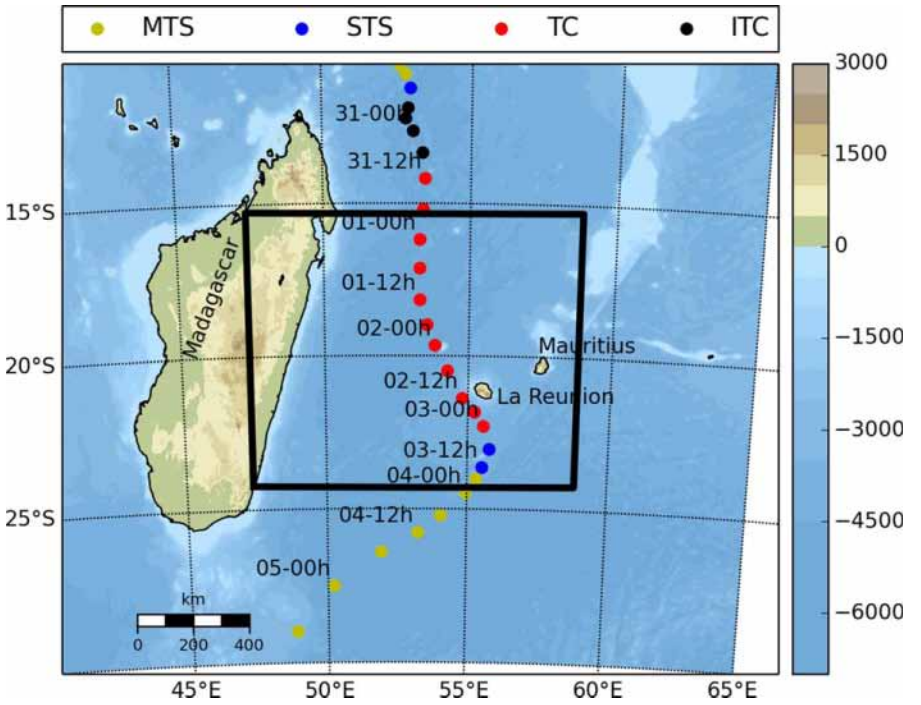

Figure 1. Orography and bathymetry (m; colors) in the domain, and best-track of Bejisa estimated by RSMC of La Réunion (colored dots). The green, blue, red, and black dots correspond to the intensity of Bejisa following the classification of RSMC La Réunion (see text for details): Moderate Tropical Storm (MTS), Strong Tropical Storm (STS), Tropical Cyclone (TC), and Intense Tropical Cyclone (ITC), respectively. The black box corresponds to the domain location for the Meso-NH, WW3 and CROCO models (cf., section 3).

altitude divergence resulted in this low-pressure system being classified as a Moderate Tropical Storm during the night of 29 December. As the vertical wind shear disappeared, the convection strengthened. A very rapid intensification phase started at 12 UTC on 29 December and lasted 24 h. This rapid intensification phase, favored by the small radius of the eye of the cyclone (diameter of about 10 km), was characterized by a 32.5 m s^{-1} increase of the 10 min averaged maximum wind speed and a deepening of the minimum central pressure by 47 hPa in 24 h, exceeding established rapid intensification thresholds (Kaplan et al., 2010). Thus, at 12 UTC on 30 December, Bejisa was classified as an Intense Tropical Cyclone with 48.9 m s^{-1} 10 min averaged maximum wind speed and 950 hPa minimum central pressure. On 31 December, as the eye diameter had increased to 25 km, the vertical wind shear started to increase while a large external rainband wrapped around the inner core of the system (Figure 2a). This eyewall replacement cycle was completed during the night. On 1 January, the cyclone was located 500 km north-northwest of La Reunion and

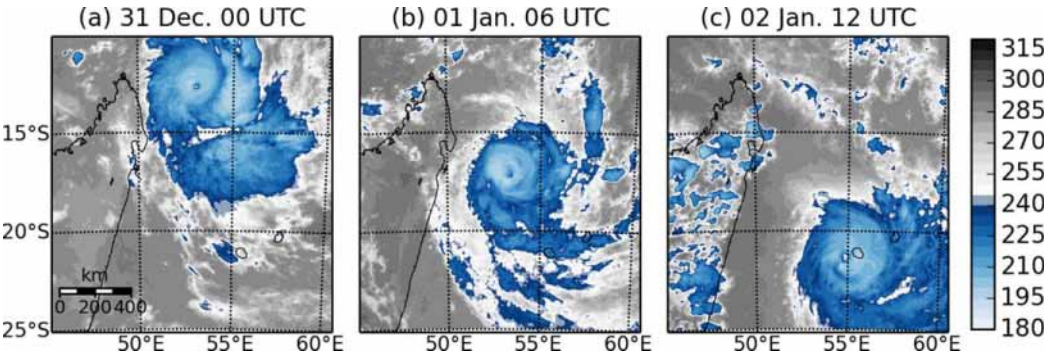

Figure 2. Brightness temperature (K) from (a) Meteosat IR channel at 00 UTC on 31 December 2013, (b) at 06 UTC on 1 January, and (c) at 12 UTC on 2 January 2014.

was propagating southward at 5.5 m s^{-1} (Figure 2b). During the next 24 h, Bejisa accelerated under the influence of a midaltitude ridge in the east. As the ridge weakened, Bejisa curved toward the south-east. On 2 January, a persisting weakness on the north to northeast side of the eyewall appeared on the scope of La Réunion radar. The radar images showed a strong instability of the eyewall while tropical cyclone Bejisa passed across the western side of La Réunion during the afternoon of 2 January (Figure 2c). The eyewall of Bejisa passed 10 km from the island at the closest. After passing La Réunion, the north-northwest part of the eyewall of Bejisa tore due to strong northwesterly winds at altitude. At 170 km to the south of La Réunion island, Bejisa was classified as a severe tropical storm and died out rapidly after turning south-southwest under the influence of a subtropical high-pressure cell located in the south of the system.

Its cyclogenesis region made Bejisa an unusual tropical cyclone that consequently affected the area (western and southwestern regions) of La Réunion. Wind gusts of less than 33 m s^{-1} were reported in the northern and eastern areas of La Réunion, and more than 41 m s^{-1} in the west and high areas of the island. The duration of the rainy period was short but intense accumulated rainfall was measured. More than 600 mm were reported in 48 h in the inner part of the island and up to 1,025 mm in Cilaos. The significant wave height of the wind and swell waves reached more than 7 m on the north-west coast of the island, which produced a strong storm surge and great damage along the west coast of the island and in the lagoon area. During this event, 180,000 people were left without electricity and 40% of the population did not have running water. The waves and river flooding caused significant damage to infrastructures in Saint Gilles. Part of the fruit production was damaged while most of vegetable crop was lost.

This study focuses on the period between 00 UTC on 1 January and 18 UTC on 2 January when Bejisa passed close to La Réunion. This period does not correspond to the most intense phase or to the rapid intensification phase but was chosen because of the interest of operational forecasts for understanding and preventing damage on La Réunion island and because of the availability of observations. It is the only period for which observations from radar, coastal buoys, and meteorological stations are available and can be used to evaluate the simulations.

3. Presentation of the Modeling System

Figure 3 shows the numerical MSWC (Meso-NH/SurfEx, WW3, and CROCO) system used in this study. These models were chosen because they can represent the fundamental processes involved in TC, from regional to coastal ones, and for deep to shallow waters. This coupling system is based on the multimodel coupling platform described in Voldoire et al. (2017), which has been extended to the use of the CROCO model. The

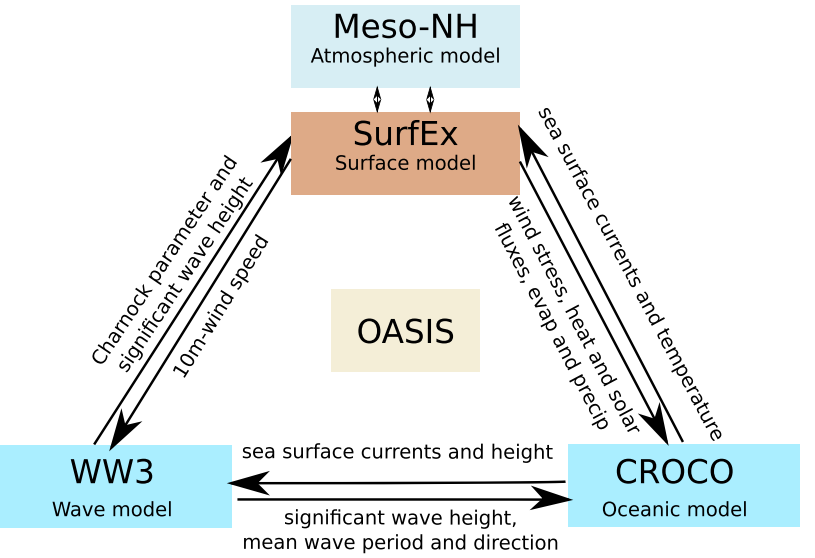

Figure 3. Schematic diagram of the coupling system. Fields exchanged among the atmospheric, wave, and oceanic models are also presented. All the parameters are exchanged at 10 min intervals.

main features and the configuration of each model are described in this section, along with the coupling strategy.

3.1. The Atmospheric Model: Meso-NH

Meso-NH is an atmospheric model developed by the Centre National de Recherches Météorologiques (Météo-France and Centre National de la Recherche Scientifique) and the Laboratoire d'Aérologie (Centre National de la Recherche Scientifique and University of Toulouse) (http://mesonh.aero.obs-mip.fr). It is a nonhydrostatic anelastic model, able to simulate the motion of the atmosphere, at scales ranging from synoptic (hundreds of kilometers) to microscale (tens of meters). Meso-NH has already been successfully used to simulate storms and tropical cyclones (Barthe et al., 2016; Chane-Ming et al., 2014; Jolivet et al., 2013; Nuissier et al., 2005; Pantillon et al., 2013, 2015, 2016).

Meso-NH has a large set of physical parameterizations to represent radiation, turbulence, clouds, precipitation, convection, chemistry, aerosols, etc. For the present study, the MNH-V5-3-0 package was used, and a simple set of physical parameterizations was chosen. The microphysics scheme (Pinty & Jabouille, 1998) was a single-moment bulk mixed-phase scheme predicting the mixing ratio of five microphysical species: cloud water, rain, cloud ice, snow, and graupel. A shallow convection parameterization based on mass-flux calculations (Bechtold et al., 2001) was used. The turbulence parameterization was based on a 1.5 order closure (Cuxart et al., 2000) with purely vertical turbulent flux computations using the mixing length of Bougeault and Lacarrère (1989). The radiative scheme was the one used at the European Center for Medium-Range Weather Forecasts (ECMWF; https://www.ecmwf.int/) (Gregory et al., 2010) including the Rapid Radiative Transfer Model (RRTM) parameterization for longwave radiation (Mlawer et al., 1997). The Organic Inorganic Log-normal Aerosol Model (ORILAM; Tulet et al., 2005) is used to simulate sea salt aerosol processes, such as emission, transport, sedimentation, and dry deposition. In this study, the sea salt aerosol size distribution consists of five log-normal modes: two modes for ultrafine sea salt aerosols (Aitken modes; radius < 0.05 μm), two others for fine sea salt aerosols (Accumulation modes; 0.05 μm $<$ radius < 0.5 μm), and an other one for coarse sea salt aerosols (Coarse mode; radius > 0.5 μm). These five log-normal modes are described by the sea salt aerosols number concentration (the number median radius and geometric standard deviation being held constant). Note that the effect of sea salt aerosols on cloud microphysics is not considered in this paper.

The surface-atmosphere interactions are grouped on a surface modeling platform, called SurfEx (Surface Externalisée in French; Masson et al., 2013; Voldoire et al., 2017). Various physical models compose SurfEx to account for natural land surface, urbanized areas, lakes, and oceans. It can be used in standalone mode or coupled to various models (ocean, oceanic waves, river, etc.). The SurfEx platform used in this study included the ISBA (Interaction Soil-Biosphere-Atmosphere; Noilhan & Planton, 1989) model, a land surface model with three soil layers by default, and the COARE (Coupled Ocean-Atmosphere Response Experiment, Fairall et al., 2003) parameterization of sea surface fluxes. This parameterization allows coupling with oceanic waves (see section 3.4).

The sea salt aerosol emission parameterization used in this study was based on that of Ovadnevaite et al. (2014) and was implemented in Meso-NH/SurfEx by Claeys (2016). This is the only parameterization that takes account of a wide range of parameters that influence the emission of sea salt aerosols: the 10 m wind speed, the significant wave height and the water viscosity through the sea surface temperature and salinity. Traditionally, sea salt aerosol emissions are parameterized by 10 m wind speed alone but the dependence of the aerosol concentration on the sea-state is evident and was confirmed recently by Lenain and Melville (2017).

The Meso-NH/SurfEx domain covers an area of 1,200 km $\times$ 1,000 km with a horizontal grid spacing of 2 km. This grid length enables deep convection to be explicitly represented, which results in a better simulated structure of the tropical cyclone (Fierro et al., 2009; Gentry & Lackmann, 2010). The vertical grid has 70 stretched levels with enhanced resolution close to the ground and in the outflow region. Associated with the leapfrog temporal scheme, momentum variables were advected with a centered fourth-order scheme, while scalar and other meteorological variables were advected with a monotonic Piecewise Parabolic Method to ensure positive values (Colella & Woodward, 1984). The time step of Meso-NH is 3 s. The simulations were performed from 00 UTC on 1 January 2014 to 18 UTC on 2 January 2014. Meso-NH/SurfEx was initialized at 00 UTC with AROME-IO analysis. AROME-IO is the AROME-Indian Ocean configuration of the

operational Météo-France model AROME. Meso-NH/SurfEx was forced at the lateral boundaries by the 6 h-ECMWF operational high-resolution analysis.

3.2. The Wave Model: WW3

The wave model WW3 (WAVEWATCH3; http://polar.ncep.noaa.gov/waves/wavewatch/; Tolman, 1992; The WAVEWATCH III Development Group, 2016) solves the random phase spectral action density balance equation for selected wavenumber-direction spectra. The effects of wind-wave interactions, nonlinear wave-wave interactions, wave-bottom interactions, depth-induced breaking, dissipation, and reflection off the shoreline are parameterized. For the present study, the third-order Ultimate Quickest scheme by Tolman (2002) with the Garden Sprinkler correction was used to avoid this numerical artifact due to the discrete directions of wave propagation. Nonlinear wave-wave interactions were modeled using the Discrete Interaction Approximation (DIA, Hasselmann et al., 1985). The wind-wave interaction source term of Ardhuin et al. (2010) was used. This parameterization is built around a saturation-based dissipation, reducing the unrealistically large drag coefficients under high winds. Additionally, depth-induced wave breaking (Battjes & Janssen, 1978) and bottom friction source terms (Ardhuin et al., 2003) were used. Finally, reflection by shorelines described in detail in Ardhuin and Roland (2012) was also activated.

The grid covered the same area as Meso-NH/SurfEx with 692 $\times$ 578 points and a spatial resolution of 1/60° ($\sim$1.7 km). The global time step of WW3 was 100 s. The spectral discretization of WW3 was 24 for the direction (every 15°) and 32 for the frequency. Along the track of tropical cyclone Bejisa, the ocean depth was roughly 4,000 m. Thus, the shallow water parameterizations were only useful close to the shoreline. A stand-alone WW3 run of 3 days, from 00 UTC on 28 December 2013 to 00 UTC on 1 January 2014 was set up to downscale from global MARC (Modélisation et Analyse pour la Recherche Côtière) hindcast (http://marc.ifremer.fr/) to our simulation domain. The horizontal resolution of the MARC hindcast is 0.5° and the spectral discretization is 24 for the direction (every 15°) and 32 for the frequency. The 10 m wind speed used to force the MARC hindcast and the stand-alone WW3 run came from the ECMWF operational high-resolution analysis. The new spectra from the stand-alone WW3 run were imposed every 3 h at the boundaries of WW3 in the coupled simulations.

3.3. The Oceanic Model: CROCO

The ocean was modeled with the Coastal and Regional Ocean COmmunity model (CROCO; http://www.croco-ocean.org). CROCO is a new model built upon ROMS-Agrif (Debreu et al., 2012; Penven et al., 2006). It includes more and more capabilities, such as OWA coupling. It is a free-surface, terrain-following coordinate model with split-explicit time stepping. It solves the incompressible primitive equations based on the Boussinesq and hydrostatic approximations and is coupled to advection-diffusion schemes for potential temperature and salinity as well as a nonlinear equation of state for density. The advection scheme is third-order upstream biased, which reduces dispersion errors, essentially enhancing precision for a given grid resolution (Shchepetkin & McWilliams, 1998). Subgrid-scale vertical mixing is introduced by the nonlocal K-profile parameterization (KPP) scheme (Large et al., 1994). The bottom stress is computed using a simple linear formulation with a constant bottom drag coefficient set to $C_d = 3.10^{-4}$. Coupling with oceanic waves is described in Marchesiello et al. (2015).

The grid covers the same area as WW3 and Meso-NH/SurfEx and with the same resolution as WW3, i.e., 1/60° ($\sim$1.7 km) with 692 $\times$ 578 points. The temporal scheme used is a time-splitting scheme with chosen baroclinic and barotropic time steps of 100 and 2 s, respectively. The bathymetry is constructed from the GEneral Bathymetric Chart of the Oceans global bathymetry (GEBCO; available online at http://www.gebco.net). To avoid pressure gradient errors induced by terrain-following coordinates in shallow regions with steep bathymetric slope (Beckmann & Haidvogel, 1993), a local smoothing of the bottom topography is applied where the steepness of the topography exceeds a factor $r = \nabla h/h$ of 0.25 (where h is the depth). The domain has 32 vertical levels, with enhanced resolution near the surface. The original vertical grid stretching formulation described in Song & Haidvogel (1994) is used.

The model is initialized and forced at its boundaries using the 3 day ECCO2 reanalysis (Estimating the Circulation and Climate of the Ocean: Phase 2, Menemenlis et al., 2008) at 00 UTC on 1 January 2014. Figure 4a shows the sea surface temperature from the ECCO2 analysis used as an initial condition for all the simulations. The colored squares represent the sea surface temperature (SST) measured by drifting buoys from the

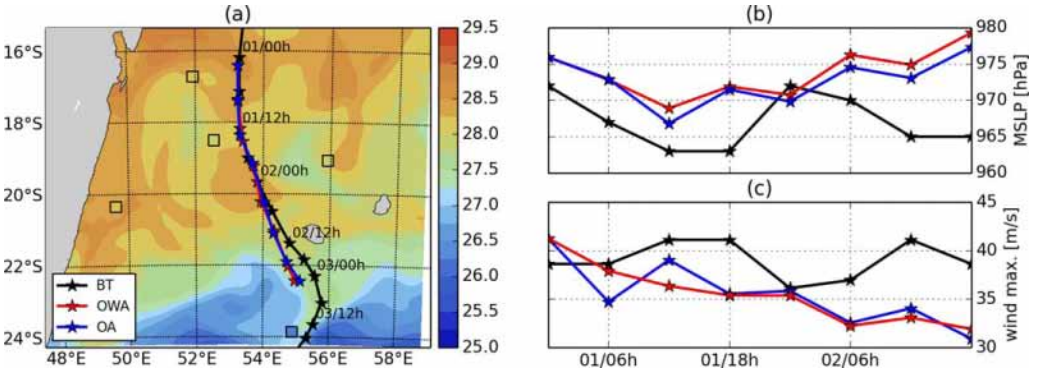

Figure 4. (a) SST (°C, colors) from the OWA simulation and from drifting buoys (WMO database; color squares) at 00 UTC on 1 January, and track of Bejisa (lines with stars). (b) Evolution of the minimum mean sea level pressure (MSLP, in hPa). (c) Evolution of the maximum sustained wind speed (in m s^{-1}). The black, red, and blue lines represent the best-track, and the OWA, and OA simulations, respectively. Each star corresponds to data at a 6 h interval.

WMO (World Meteorological Organization) database at the same time. Overall, the sea surface temperature observed by the drifting buoys is well reproduced by the analysis. A latitudinal gradient is shown in the sea surface temperature pattern, going from hotter sea surface temperatures in the north (∼29°C at 16°S) to colder ones in the south (∼26°C at 24°S). The difference between the ECCO2 analysis and the drifting buoys in the south of the domain is higher than in the north, where the sea surface temperature pattern is better reproduced. Overall, the sea surface temperature from the ECCO2 analysis reproduces the sea surface temperature from drifting buoys with less than a ∼0.2°C difference, making this analysis suitable to initialize the oceanic model.

3.4. Coupling Strategy

OASIS (Ocean Atmosphere Sea Ice Soil, Craig et al., 2017) was used to couple the oceanic, waves, and atmospheric models. The current OASIS3-MCT version is interfaced with the Model Coupling Toolkit (MCT, Jacob et al., 2005; Larson et al., 2005) and with the Spherical Coordinate Remapping Interpolation Package (SCRIP, Jones, 1999). OASIS3-MCT is fully parallelized, allowing very good computational performance. The variables that are exchanged between the various models are shown in Figure 3.

In SurfEx, turbulent fluxes at the sea surface are computed using the sea surface temperature (SST; K) and the two components of the sea surface currents (m s^{-1}) from CROCO. These parameters are used to compute the stability of the atmosphere and the relative wind. The Charnock parameter (α; dimensionless) (Charnock, 1955) from WW3 is also needed. In WW3, the Charnock parameter is computed using the Janssen (1991) formulation $\alpha = 1/\sqrt{1-\tau_w/\tau}$, with τ_w the wave-induced stress including the resolved part of the spectrum and τ the total stress. The Charnock parameter is used in SurfEx to compute the roughness length formulation (z_0; m) following Smith (1988):

$$z_0 = \alpha \frac{u_*^2}{g} + 0.11 \frac{\nu}{u_*}, \tag{1}$$

where ν is the cinematic viscosity of the air (15.6×10^{-6} m^2 s^{-1} at the ground) and g the gravitational acceleration (9.81 m s^{-2} at the ground). u_* is the friction velocity (m s^{-1}) defined as:

$$u_* = u \frac{\kappa}{\ln\left(\frac{z}{z_0} - f\left(\frac{z}{L_{MO}}\right)\right)}, \tag{2}$$

where κ, u, and z are the Von Kàrmàn constant (dimensionless value of 0.4), the relative wind speed (difference between the wind speed at the first level and the sea surface currents from CROCO) (m s^{-1}) and the height (m), respectively. $f(z/L_{MO})$ is a stability function based on Monin-Obukhov theory (dimensionless) and L_{MO} is the Monin-Obukhov length (m). These equations are solved using an iterative method. After convergence (less than five iterations), z_0 and u_* are used to compute the transfer coefficients, a component of the turbulent surface fluxes, which are the surface boundary conditions of the Meso-NH model. Without wave coupling, the Charnock parameter depends on the 10 m wind speed (Hare et al., 1999):

$$\alpha = 0.011 \quad \text{if} \quad u < 10 \text{ m s}^{-1},$$
$$\alpha = 0.011 + 0.007\frac{u-10}{8} \quad \text{if} \quad 10 \text{ m s}^{-1} < u < 18 \text{ m s}^{-1}, \tag{3}$$
$$\alpha = 0.018 \quad \text{if} \quad u > 18 \text{ m s}^{-1}.$$

Such a parameterization takes into account the oceanic waves by (1) increasing the Charnock parameter linearly with wind between 0.011 and 0.018 (increasing steepness of the waves with wind speed) and (2) saturating the Charnock parameter at high winds (impact of wave breaking and sea spray). Sensitivity experiments, made in this study and presented in section 3.5, investigate the impact of using a Charnock parameter computed from the wave model against such a parameterization.

Sea salt aerosol fluxes are computed using the significant wave height, H_s, from WW3 and SST from CROCO. Note that the effects of sea salt on turbulent air-sea fluxes and on cloud microphysics are not considered in this paper and will be addressed in a future study.

The wind-waves parameterization of Ardhuin et al. (2010) in WW3 is computed using the two components of the 10 m wind speed from SurfEx and the two components of the sea surface currents and sea surface height from CROCO. It must be noted that WW3 computes its own momentum flux using the 10 m wind speed from SurfEx. This computation is based on a bulk formulation under neutral atmospheric conditions and a subtle balance between wave growth and wave dissipation. Therefore, consequent changes in WW3 source term parameterization would be necessary to use SurfEx wind stress instead of 10 m wind speed. This will be done in a future study. The inconsistency between SurfEx and WW3 momentum flux is evaluate to be about 10% in very localized high wind speed maxima and less than a few percentages around (not shown here).

Surface boundary conditions of the oceanic model use the solar flux, the net heat flux, and the evaporation and precipitation terms from SurfEx. Momentum flux is also prescribed from SurfEx directly. Wave-to-ocean momentum flux is computed in WW3 but as an inconsistency exists between WW3 and SurfEx momentum formulation, it has been considered that SurfEx flux was more accurate as it takes into account all the atmospheric boundary layer processes. Another possibility would have been to prescribe as surface stress the wave to ocean momentum flux (computed from WW3) plus the remaining stress not used for wave growth (SurfEx stress minus WW3 stress). This has been tested and gave very similar results than prescribing directly SurfEx wind stress (not shown here). The wave-ocean interaction terms (Marchesiello et al., 2015) like the Stokes drift and the nonbreaking waves induced mixing following Uchiyama et al. (2009) are computed using the from WW3.

All models used in this study (Meso-NH/SurfEx, WW3, and CROCO) had the same domain location (see the black box in Figure 1). All surface fields were exchanged every 10 min and were interpolated from grid to grid through distance weighted nearest-neighbor interpolation with four neighbors using OASIS libraries.

3.5. Set of Experiments

A set of seven experiments was performed (Table 1) to highlight the impact of oceanic waves on the tropical cyclone evolution and on the sea salt aerosol emissions. The reference experiment was the fully coupled Ocean-Waves-Atmosphere (OWA) simulation where all the fields were exchanged. Sea salt aerosol fluxes were computed from the Ovadnevaite et al. (2014) parameterization described in section 3.1 and used the significant wave height (H_s) from WW3.

Table 1
List of Numerical Experiments

Experiments	WW3 coupling	H_s used in the sea salt aerosol fluxes parameterization
OWA	X	H_s from WW3 (online coupling)
OA		
OWA_2m	X	H_s homogeneous, constant, and equal to 2 m
OWA_9m	X	H_s homogeneous, constant, and equal to 9 m
OWA_MARC	X	H_s from MARC global hindcast
OWA_FORC	X	H_s from WW3 stand-alone run (offline coupling)
OWA_ERAI	X	H_s from ERA-Interim

Six additional simulations were performed. The first sensitivity experiment was the Ocean-Atmosphere (OA) simulation, where the wave model was removed and the Charnock parameter was computed using the Hare et al. (1999) parameterization (equation (3)). The impact of oceanic waves coupling (comparison between the OWA and OA simulations) is presented in section 5.

The other five simulations were similar to the OWA simulation but the significant wave height (H_s) used in the sea salt aerosol flux computation was different. For the OWA_2m and OWA_9m, the H_s used in the sea salt aerosol fluxes is homogenous, constant, and equal to 2 and 9 m, respectively. These values were chosen because they represent the minimum and maximum values encountered in the spatial

distribution of H_s in the OWA simulation (see section 4.3). For the OWA_ERAI experiment, the H_s used in the sea salt aerosol fluxes were extracted from the ERA Interim reanalysis (Berrisford et al., 2011). ERA-Interim data are a global atmospheric reanalysis with a spatial resolution of approximately 80 km. The horizontal resolution of these data is low but they are the only data that can be accessed via the public server of the ECMWF. For the OWA_MARC experiment, the H_s used in the sea salt aerosol fluxes was extracted from the MARC hindcast described in section 3.2. For the OWA_FORC experiment, the H_s used in the sea salt aerosol fluxes was extracted from a stand-alone WW3 run at the same resolution as the OWA simulation. This stand-alone WW3 run was forced by the 10 m wind speed of the ECMWF operational high-resolution analysis. The impact of the significant wave height on sea salt aerosol fluxes and concentration is presented in section 6.

4. Description of the Fully Coupled OWA Simulation

The aim of this section is to describe and evaluate the fully coupled OWA simulation with available observations and the literature. Best-track data are used for the evaluation of the TC track and intensity (section 4.1), buoys, and altimeters for the evaluation of the sea state (section 4.3), and drifting buoys for the evaluation of the sea surface temperature (section 4.4).

4.1. Track and Intensity

The cyclone track and intensity from the OWA simulation and from the Best-Track (BT) of RSMC La Réunion are shown in Figure 4. Best-track data are the best estimate of the characteristics of Bejisa using all the observations and models available. It includes the position (latitude and longitude) and the intensity (mean sea level pressure and maximum sustained wind speed) of the storm at 6 h intervals.

The OWA simulation (red line) reproduces the best-track (black line) closely until 00 UTC on 2 January. After that, the simulated cyclone accelerates, following a south-south-eastern direction while the observed storm moves more slowly toward the south-east. Consequently, the simulated system is located 60–70 km northwest of the estimated position of the analyzed system on 2 January between 06 UTC and 12 UTC. At the end of the simulation, the simulated cyclone decelerates as already described in section 2. Figures 4b and 4c show the temporal evolution of the minimum value of the mean sea level pressure (MSLP) and the maximum sustained wind speed, respectively. Overall, the simulated tropical cyclone is less intense than the best-track one. At the beginning of the simulation, the MSLP in the model is 976 hPa, close to the MSLP in the AROME-IO analysis (975 hPa), while the best-track MSLP is 972 hPa. The trend of the MSLP and the maximum sustained wind speed is fairly well reproduced by the model on 1 January. Starting from 00 UTC on 2 January, the intensity diverges between the simulation and the best-track. The intensity in the OWA simulation decreases by 9 hPa and 6 m s^{-1} in 18 h, while the intensity of the best-track increases by 7 hPa and 5 m s^{-1}, during the same period. Despite an underestimation of its intensity probably associated to an underestimation already present in AROME-IO initialization field, the position of Bejisa and the temporal changes of its intensity are fairly well reproduced by the OWA simulation: maximum error (before the divergence of the tracks) of 7 hPa and 6 m s^{-1} for a cyclonic system reaching 963 hPa and 41 m s^{-1}.

4.2. 10 m Wind Speed

The horizontal structure of the simulated OWA cyclone is described through the temporal evolution of the 10 m wind speed (Figures 5a, 5c, and 5e). Note that the quadrants are defined with respect to the tropical cyclone's motion: the left quadrants mean to the east of the TC. This convention is used in the following.

At 18 UTC on 1 January (Figure 5a), the eye of the cyclone is clearly visible with a weak 10 m wind region (less than 10 m s^{-1}). The surrounding eyewall exhibits the maximum 10 m wind speed ($>$ 36 m s^{-1}) in the left and right quadrants of the system. At 06 UTC on 2 January (Figure 5c), the simulated system is located as close as possible to La Réunion. Its intensity has decreased (Figure 4b) and the region of maximum 10 m wind speed ($>$ 30 m s^{-1}) is now located in the front left quadrant of the system and is close to La Réunion ($\sim$50 km). The northern part of the eyewall shows a relative weakness with 10 m wind of less than 27 m s^{-1}. At 18 UTC on 2 January (Figure 5e), Bejisa is partially broken in its northwestern region as observed (see section 2), inducing a strong asymmetry of the 10 m wind speed. It barely exceeds 27 m s^{-1} at some very localized points. Overall, the TC simulated by the OWA simulation reproduces the horizontal structure and the main behavior of tropical cyclone Bejisa, as described in section 2.

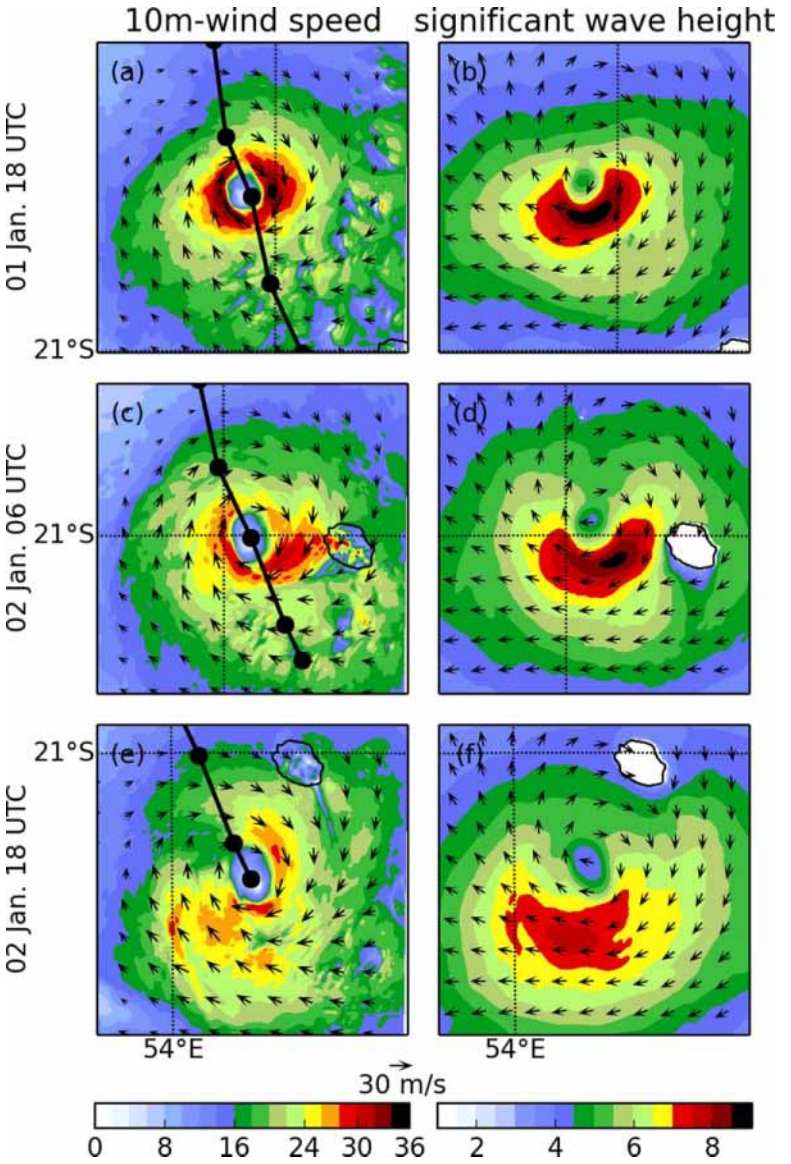

Figure 5. (left plots) 10 m-wind speed (m s^{-1}; colors) and (right plots) significant wave height for wind and swell waves (m; colors) at 18 UTC on 1 January (first row), at 06 UTC on 2 January (second row), and at 18 UTC on 2 January UTC (third row) for the OWA simulation. Black arrows correspond to the 10 m-wind speed vectors and to the wave direction in the left and right columns, respectively.

4.3. Significant Wave Height

Significant wave height is one of the key parameters involved in storm surge but also in oceanic mixing, and in the sea salt aerosol source function (section 3). In this section, H_s simulated by the OWA simulation is evaluated through comparisons with buoy and altimeter data.

Figures 5b, 5d, and 5f show the temporal evolution of the H_s in the OWA simulation. Overall, the main oceanic waves (Figures 5b, 5d, and 5f) are localized under the cyclone eyewall (Figures 5a, 5c, 5e), meaning that they are directly generated by the cyclonic wind and are not advected from outside the simulation domain. At 18 UTC on 1 January, the main wave packet has a maximum value of H_s higher than 8 m, located in the front quadrants of the cyclone. This wave packet propagates to the south with a bean-like structure. This is well-known behavior for waves associated with tropical cyclones, based on theoretical considerations (Cline, 1920), numerical modeling (Chen & Curcic, 2016; Moon et al., 2003) and in situ observations from ships (Tannehill, 1936), airplane (Wright et al., 2001), and buoy measurements (Esquivel-Trava et al., 2015).

This shape results from the higher wind speed in the quadrant associated with the forward motion of the storm. An additional mechanism is the increase of the effective fetch and the duration of the wave-growth process in the direction of the motion of the storm (Wright et al., 2001). Twelve hours before the cyclone reaches La Réunion, oceanic waves with H_s of about 3–4 m touch the northern side of the island. The wave direction turns clockwise, like the main wind direction. As noted by Wright et al. (2001), the dominant waves propagate at a more or less large angle to the 10 m wind. In the right quadrants of the system, this angle is maximum. When the cyclone is close to the western coast of La Réunion (Figure 5d), the maximum of significant wave height is close to 9 m. After passing La Réunion island, H_s decreases at the same time as the cyclone intensity (Figures 5e and 5f). Since the oceanic waves also propagate to the north, behind the cyclone, the southern side of La Réunion is impacted by the swell several hours after the passage of the cyclone (Figure 5f). Analyzing the microseismic noise using permanent and nonpermanent seismic stations, Davy et al. (2016) showed that microseismic noise was still giving a recordable signal when Bejisa was located south of the island confirming the presence of northward swell after the passage of the TC.

To evaluate the H_s simulated by the OWA simulation, a comparison with buoy data is made and presented in Figure 6. Direct observations are available from nondirectional ocean wave gauges of the CANDHIS (Centre d'Archivage National de Données de Houle In Situ; http://candhis.cetmef.developpement-durable.gouv.fr/) network (CANDHIS_97403) and from two buoys (NRL_RN2 and NRL_RN4) that were temporarily installed on the north-west shore of La Réunion (Figure 6a).

Three different stages can be distinguished on each site. From 00 to 22 UTC on 1 January, the storm is located north of the island and relatively far from it, and H_s is increasing slightly on the north of the island. At the beginning of the simulation, H_s is between 1 and 1.2 m in the model, and between 0.8 and 1 m in the observations. It increases by approximately 2 m in 22 h both in the observations and in the model. During this first stage, the model is in very good agreement with observations. From 22 UTC on 1 January to 06 UTC on 2 January, Bejisa is approaching La Réunion, and H_s increases significantly (1.5–2 m in 8 h). In the simulation, the maximum of H_s is reached at 06 UTC on 2 January for the NRL_RN2 (5.8 m) and NRL_RN4

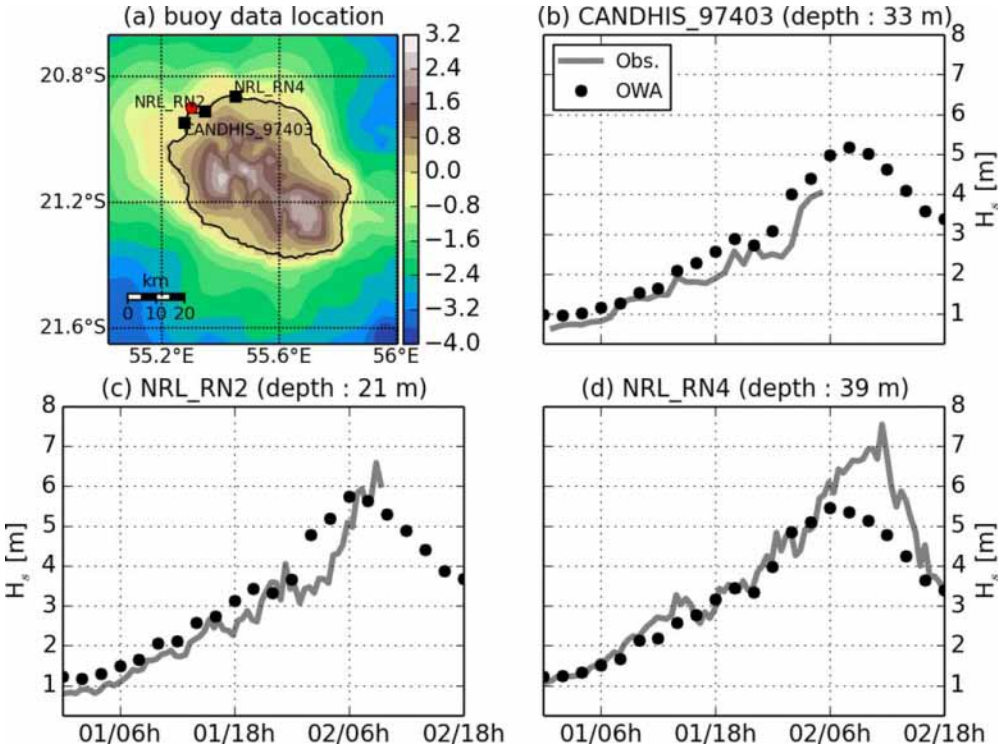

Figure 6. (a) Position of the three buoys (black squares) and bathymetry/orography (km; colors) around La Réunion. The red dot corresponds to Pointe des Galets. Evolution of the H_s (m) at the (b) CANDHIS_97403, (c) NRL_RN2, and (d) NRL_RN4 buoy locations. The gray line shows the observations while the black dots display the results of the OWA simulation.

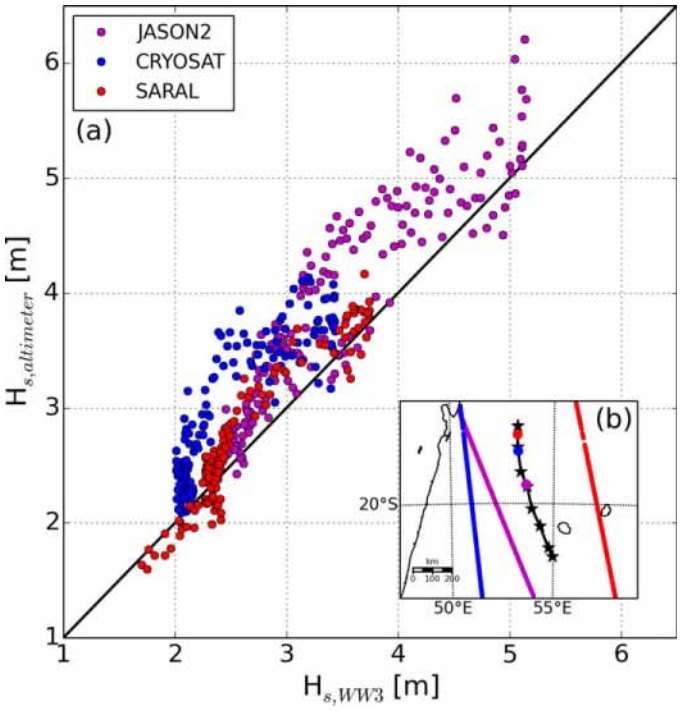

Figure 7. (a) Scatterplot of the significant wave height (m) from altimeters versus collocated significant wave height (m) from the OWA simulation. (b) Location of the satellite tracks in the domain location. Black stars correspond to the simulated track of the OWA simulation, every 6 h from 00 UTC on 1 January to 18 UTC on 2 January. Color dots correspond to the position of the simulated TC at the different altimeters crossing times (Jason-2 at 17 h 15 min UTC on 1 January, Cryosat: 7 h UTC on 1 January and Saral at 2 h 30 min UTC on 1 January). Each satellite crosses the domain in approximately 2 min.

(5.5 m) buoys, and 2 h later for the CANDHIS_97403 buoy (5.1 m). Note that the CANDHIS_97403 and NRL_RN2 buoys broke during the cyclone and did not measure the wave peak. For the remaining NRL_RN4 buoy, the model differs from the buoy data concerning the time and value of the peak of H_s. It is 5 h in advance in the simulation (06 UTC on 2 January) compared to the observations (11 UTC on 2 January). This is in agreement with a simulated system traveling faster than the observed one (Figure 4). Moreover, the simulated peak of H_s (5.5 m) is lower than the observed one (7.6 m). This is in agreement with the larger distance of the center of Bejisa from La Réunion in the simulation (∼70 km) compared to the best-track (∼50 km; Figure 4a). This could also be explained by (i) the low-resolution of the wave model that does not resolve the shallow water processes in the vicinity of the coast well (the depth at buoys location is less than 40 m for observations and close to 100 m for OWA simulation), (ii) the proximity of the buoys to the coast (less than 1 km off the coast), and (iii) the 1.7 km resolution of the wave model, which that makes comparison with these buoys delicate. During the third stage, Bejisa is moving away from the island, and the northern coast is becoming more and more protected from the cyclonic swell, leading to a decrease in H_s. The maximum H_s for the CANDHIS_97403 buoy is lower than for the other two buoys although Bejisa passed closer to this buoy. In fact, it was relatively protected by Pointe des Galets (red dot in Figure 6), and the plateau west of the buoy increased the friction, and consequently the wave breaking, leading to lower values of H_s.

To assess the simulated H_s from the OWA simulation, a comparison is also made with the data from altimeters (in Figure 7 and Table 2).

The merged and calibrated altimeter data set of Queffeulou and Croizé-Fillon (2017) is used in this study. Data from the Cryosat, Jason-2, and Altika Saral missions are available for the relevant period and region of interest and are presented in Figure 7b. Only the altimeter data in the offshore areas (further than 50 km from the coast) were taken into account, as comparisons with coastal buoy measurements indicated biases and errors in the altimeter measurements (Shanas et al., 2014), especially because of the large antenna footprint. The three altimeters' bands cover an area localized around the TC (more than 100 km from the TC center; Figure 7b), which allows an evaluation of the deep water external region of the TC. There, the H_s is not maximum and not influenced by the shallow water processes. Standard error statistics are computed to have a quantitative assessment of the OWA simulation. These statistics include the correlation coefficient (R), the bias (bias), and the root mean square error (rmse; Table 2).

The correlation coefficient is close to 1 (0.99) for all altimeter data. This means that temporal and spatial variability of the simulated H_s are highly correlated with the H_s measured using the altimeters. Regarding the bias, the simulated significant wave height is underestimated by 34 cm (less than 10%) compared to the altimeter measurements (Table 2). However, some discrepancies between altimeters can be noted. This bias is higher for comparisons with Cryosat and Jason-2 (respectively, 43 and 48 cm) which is consistent with the underestimation of the simulated H_s under TC, shown in Figure 6. Comparison of the simulated H_s with Saral altimeter shows a weaker bias of less than 11 cm (3.5%). At the time and location of Saral measurement, the simulated H_s is not yet influenced by oceanic waves generated by the simulated TC but only by preexisting wave field. This could explain the lower bias of the simulation compared to Saral than to other altimeters. Spreading of the data is now evaluated with the rmse. For Cryosat and Jason-2, the rmse is 57 cm while it does not exceed 23 cm for the Saral Altimeter. This shows that the H_s error

Table 2
Statistical Metrics (Correlation Coefficient (R), bias, rmse) of Differences Between H_s From Altimeters and OWA Simulation

Satellite	Jason-2	Cryosat	Saral	All
R	0.99	0.99	0.99	0.99
bias (cm)	−43	−48	−11	−34
rmse (cm)	57	57	23	46

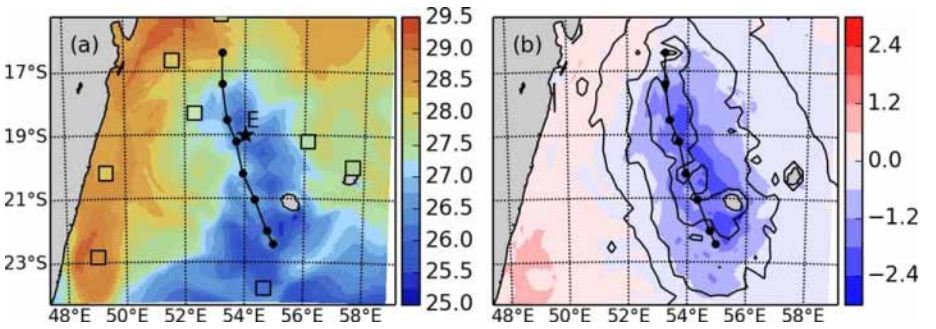

Figure 8. (a) SST (°C, colors) from the OWA simulation and drifting buoys (colored squares) at 18 UTC on 2 January. (b) Difference between the SST at 18 UTC on 2 January and at 00 UTC on 1 January (Figure 4a). The black line with dots corresponds to the track of the cyclone in the OWA simulation. In plot (b), the black contours correspond to the mean momentum flux during the OWA simulation (contours at 0.2, 0.4, and 0.8 kg m^{-1} s^{-2}). The black star on plot (a) (point (E)) is the point where vertical profiles of temperature and currents were extracted.

does not deviate by more than 60 cm from the regression line, leading to the conclusion that simulated H_s variability is in quite good agreement with H_s variability from satellites.

Overall, the significant wave height simulated by the OWA simulation is in good agreement with buoy and satellite observations, with a difference of less than 10% for big waves.

4.4. Sea Surface Temperature

Sea surface cooling under a tropical cyclone is one of the air-sea coupling processes involved in tropical cyclone evolution. To evaluate the simulated sea surface cooling, the final SST of the OWA simulation is presented in Figure 8a.

A colder SST region (26–27°C) clearly appears along the track of Bejisa, while the SST in the surrounding waters is higher than 27.5°C north of 22°S. The simulated SST is in good agreement with the data from the drifting buoys (WMO database) in the external part of the cold wake. For each buoy, less than 0.25°C difference is reported between the observation and the simulation. The difference in the SST between the end (18 UTC on 2 January) and the beginning (00 UTC on 1 January) of the simulation is shown in Figure 8b. Because of the asymmetric wind stress forcing, the SST cooling is highly asymmetric and is maximum on the left quadrants. The sea surface temperature measured from satellites exhibits this same qualitative structure but the presence of clouds makes the comparison with this simulation difficult and it is not shown here. Two combined effects explain this asymmetry. First, the addition of the strong tangential winds on the left side of the system combined with the translation speed induces more wind stress and increases oceanic vertical mixing. In addition, currents are also increased by inertial resonance, localized at the same place, with the winds. These processes result in a cooler SST on the left side of the TC and contribute to the asymmetry of the system. They have been largely modeled and observed (D'Asaro et al., 2007; Jullien et al., 2012; Price, 1981). Along the entire cyclone track, the SST cools by more than 0.6°C over a distance of 200 (100) km on the left (right) side of the system. It can be seen that the 0.4 kg m^{-1} s^{-2} contour of the mean momentum flux is well collocated with the −0.6°C cooling rate. The maximum cooling is between 1.8 and 2.4°C and persists for more than 24 h after the passage of Bejisa. It occurs in a 40 km wide band centered 50–100 km left of the system.

4.5. Oceanic Boundary Layer Evolution

To explain the SST cooling visible in Figure 8, the temporal evolution of the thermocline and of the oceanic currents was examined. Vertical profiles were extracted at the point (E) shown by a black star in Figure 8a. This point was located in the region where cooling was maximum and upstream of La Réunion to highlight the response of the thermocline after the passage of Bejisa. Figure 9 shows the temporal evolution of the mean sea level pressure and of the vertical profiles of temperature and currents extracted at this point.

For the first 15 h, the system is north point E (Figure 8a). The SST is around 28°C and the thermocline is located at 55–60 m depth (Figure 9b). Between 15 and 25 h of simulation, while the storm passes close to the point E (where the MSLP is minimum in Figure 9a), the SST decreases from 28°C to less than 26.5°C. It

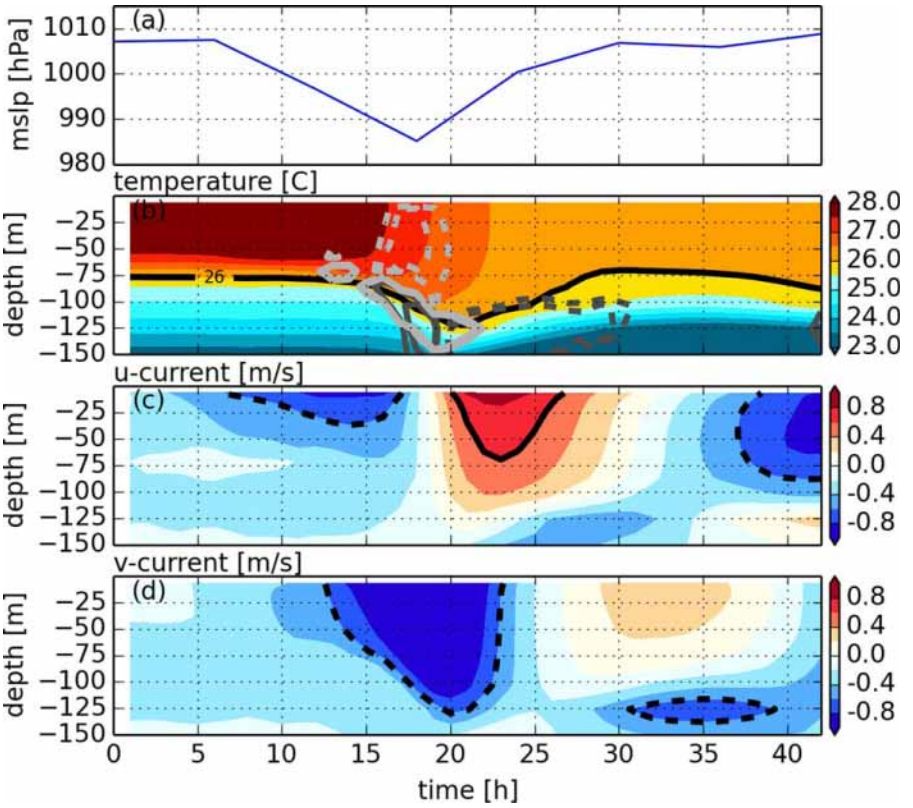

Figure 9. Time series of (a) the mean sea level pressure (MSLP; hPa), and of the vertical profiles of (b) the oceanic temperature (°C), and (c) the *u*, and (d) *v* components of the oceanic current (m s^{-1}). In plot (b), the 26°C isotherm is drawn with a black isoline. The dashed and solid contours correspond to the −4, −3, 3, and 4°C d^{-1} isolines for the vertical mixing (light gray) and total advection terms (dark gray) of the temperature budget, averaged over 1 h. In plots (c) and (d), the dashed and solid contours correspond to the −0.6 and 0.6 m s^{-1} isolines, respectively. All these variables are extracted from the point (54.0°E, 19.0°S) represented with a black star in Figure 8a.

noteworthy that the maximum cooling of the SST occurs more than 5 h after the passage of the tropical cyclone. The thermocline goes down to 120 m depth at 21 h of simulation. As the cyclone approaches the point E, the depth of the oceanic boundary layer (OBL) increases, mainly because of the vertical mixing (light gray in Figure 9b) (Price, 1981). Temperature decreases by more than 3°C over 75 m. After the passage of the cyclone, the depth of the OBL decreases by strong advection (dark gray in Figure 9a) showing that Bejisa was not strong enough to entirely erode the thermocline (Zambon et al., 2014). This behavior is similar to the upper ocean response during typhoon Kalmaegi (2014) (Zhang et al., 2016).

At the beginning of the simulation, the *u*-component of the oceanic current is negative (east-west direction) between 0 and 150 m and increases from −0.3 to −0.8 m s^{-1} at the surface while Bejisa is approaching the point E (Figure 9c). The maximum is reached after 14 h of simulation, i.e., 4 h before the cyclone is at its closest to point E. After 18 h of simulation, as the eyewall passes and the wind shifts, the *u*-component of the oceanic current changes sign and becomes positive (west-east direction) with a maximum of 0.8 m s^{-1} reached after 22 h of simulation. After 30 h (12 h after the passage of the cyclone), the *u*-component of the current changes sign again and becomes negative. The *v*-component of the oceanic current is also negative (south-north direction) during the first part of the simulation and increases from −0.2 to −0.8 m s^{-1} between the surface and 110 m depth. The simulated system passes close to the point E at 18 UTC on 1 January (Figure 9a). Since the track of Bejisa is north-south, the *v*-component of the oceanic current changes sign later than the *u*-component (∼25 h). An inertial oscillation of the *u* and *v*-components of the oceanic current with a period of ∼1 day is visible between 0 and 100 m depth (Figures 9c and 9d). This result is similar to the point S2 over deep water in the ocean-atmosphere-wave coupled simulation of Hurricane Ivan in Zambon et al. (2014).

This first evaluation of the fully coupled OWA simulation of Bejisa shows good agreement with the available observations. The associated physical processes are in accordance with the literature. In particular, MSWC reproduces well the location and evolution of waves along the northern coast of La Réunion. In addition, the oceanic cooling wake is well simulated, as is the inertial oscillation of the oceanic current.

5. Sensitivity Analysis to Oceanic Waves Coupling

In order to highlight the impact of oceanic waves coupling on the evolution of the tropical cyclone, the OWA and OA simulations (see Table 1) are compared.

5.1. Track and Intensity

To identify the impact of oceanic waves coupling on the atmosphere, storm track, and intensity from the OA and OWA simulations are compared (in Figures 4a and 4b). It appears that including a wave model does not have a significant impact on the simulated tropical cyclone track for this case study (Figure 4a). However, the minimum MSLP is 0–2.5 hPa lower for the OA simulation than in the OWA simulation (Figure 4b). Thus, including the wave model acts to reduce the intensity of the cyclone slightly. This result is consistent with previous studies (Lionello et al., 1998; Liu et al., 2011, 2012) and was attributed to the increase of the sea surface roughness by oceanic waves (next section). In Wada et al. (2012) and Zambon et al. (2014), the authors attributed this to the increase of the oceanic vertical mixing by oceanic waves. In the present study, this effect is negligible compared to the increase of sea surface roughness and will not be detailed here. It is important to recall that the effects of sea salt on turbulent surface fluxes and cloud microphysics are not taken into account despite their potential impact on TC intensity (Fan et al., 2016; Zhao et al., 2017).

5.2. Charnock Parameter and Roughness Length

The Charnock parameter is a key parameter in waves-atmosphere coupling since it is used in the roughness length formulation (equation 1). To highlight the impact of the oceanic waves coupling on the Charnock parameter and roughness length computations, the spatial distribution of these parameters for the OA and OWA simulations are shown on Figures 10a and 10d and Figures 10b and 10e, respectively. Figures 10c and 10f present scatterplots of the Charnock parameter and the roughness length as a function of the relative wind speed (horizontal wind speed at first level of the atmospheric model minus sea surface current).

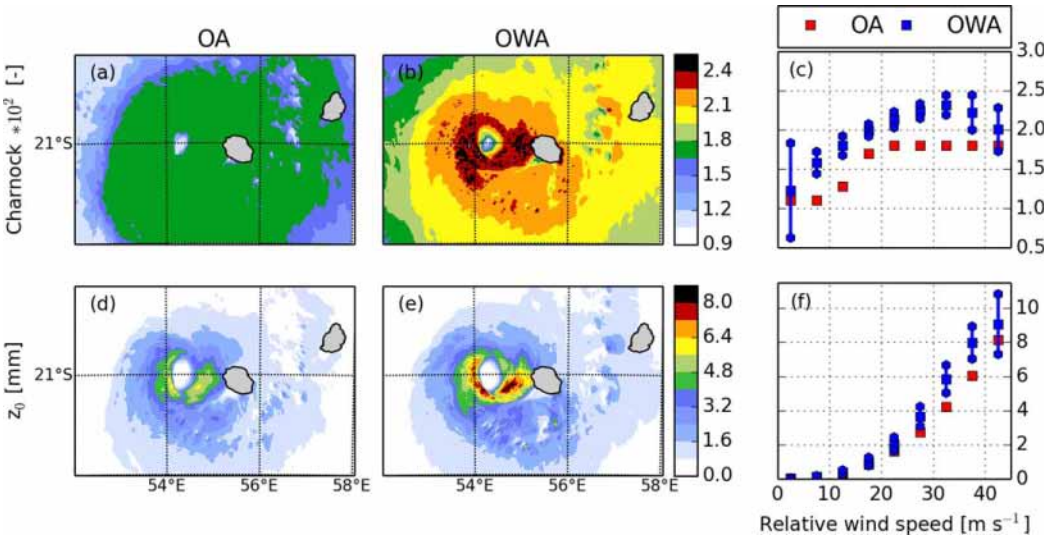

Figure 10. (left plots) Charnock parameter (w/o unit; first row) and roughness length (mm; second row) at 06 UTC on 2 January 2014 for the OA and (middle plots) OWA simulations. (right plots) Scatterplot of the Charnock parameter and roughness length versus relative wind speed. Blue and red squares correspond to mean values and blue diamonds correspond to the standard deviation.

In the OA simulation, the Charnock parameter is computed from the Hare et al. (1999) parameterization (equation (3)). Since the Charnock parameter is constant and equal to 0.018 for 10 m wind speed higher than 18 m s^{-1}, no spatial variability of this parameter is observed in the inner core of the system in the OA simulation (Figures 10a and 10c). In the OWA simulation, the spatial variability of the Charnock parameter (Figure 10b) is closely related to the 10 m wind speed distribution (Figure 5c). Moreover, it allows the sea state history to be considered from young to mature oceanic waves, represented by the standard deviation (blue diamonds on Figure 10c). It varies from 0.019 to 0.025 under the TC (Figure 10b). In the eye of the TC and for both simulations, the weak 10 m wind speed induces a low Charnock parameter. The maximum of the Charnock parameter is located in the eyewall region where the maximum values are twice as high in the OWA simulation (Figure 10b) as in the OA simulation (Figure 10a). Furthermore, a scatterplot of Charnock parameter versus of the relative wind speed (Figure 10c) shows that, for low and high relative wind speed, the Charnock parameter can vary by a factor of 2 due to the history of the sea state.

As the Charnock parameter is used to compute the roughness length (z_0), the impact of the wave coupling can also be seen on its spatial variability and extreme values (Figures 10d–10f). In the OA simulation, z_0 is between 4.8 and 5.6 mm in the eyewall and barely exceeds 5.6 mm at some points (Figure 10d) while, in the OWA simulation, z_0 exceeds 5.6 mm and even reaches 8 mm in the eyewall (Figure 10e). The scatterplot of roughness length versus the relative wind speed (Figure 10f) shows that the sea state history is only visible on the high relative wind speed ($>$ 25 m s^{-1}). This can be explained by the fact that, at low wind speed, the roughness length is controlled by the viscosity term in equation (1) and is therefore not sensitive to the Charnock parameter. Thus, the oceanic waves coupling significantly modify the roughness length at high wind speed even if the impact on tropical cyclone intensity (Figure 4b) and on the 10 m wind speed (not shown here) is mitigated. The length of the simulations might be too short to highlight the effect of oceanic wave coupling on TC structure, intensity, and track.

5.3. Turbulent Surface Fluxes

To explain the mitigated effect of oceanic waves on the TC intensity, the averaged turbulent momentum flux (τ; in kg m^{-1} s^{-2}), sensible heat flux (H; in W m^{-2}), and latent heat flux (LE; in W m^{-2}) are presented in Figure 11.

These horizontal cross-sections were obtained by reorienting the TC along the direction of motion. Then, an average was taken for momentum and heat fluxes during the simulated period. The direction of propagation is represented by the black arrows. Spatial variability of the turbulent surface fluxes given by the OWA simulation (Figures 11a, 11c, and 11e) is quite similar to that of the instantaneous roughness length (Figure 10e). Strong asymmetry is present in the turbulent surface fluxes given by the OWA simulation. Larger turbulent fluxes are located in the forward right quadrant. There, the momentum flux is about 4 kg m^{-1} s^{-2}, the sensible heat flux is 150 W m^{-2} and the latent heat flux is 600 W m^{-2}. In the opposite quadrant (rear left), values are, respectively, 3.5 (10%), 50 (30%), and 450 (25%) W m^{-2}. This asymmetry in the turbulent surface fluxes is directly linked to the cooling wake induced by the TC (Figure 8). Where cooling is maximum, the turbulent surface fluxes are reduced. For the momentum and latent heat fluxes, only the stability of the atmosphere is used, inducing a lower effect than for the sensible heat flux. For the latter, the cooling effect is greater because temperature gradient is also taken into account in its computation.

The difference between the OWA and OA simulations show the impact of oceanic waves on turbulent surface fluxes (Figures 11b, 11d, and 11f). The outstanding effect is an increase of turbulent surface fluxes in the rear-left quadrant of the TC. It is in opposition with the decrease of the fluxes due to the SST cooling wake (Figures 11a, 11c, and 11e). Globally, oceanic waves produce averaged turbulent surface fluxes that are approximately a tenth of kg m^{-1} s^{-2} or W m^{-2} stronger. This is mainly attributed to the Charnock parameter and roughness length being larger in the OWA simulation than the OA one (Figures 10c and 10f). However, divergences in turbulent flux parameterizations at high wind speeds imply a need to revisit them (Lebeaupin Brossier et al., 2008; Seyfried et al., 2017) and meaning that this sensitivity of turbulent fluxes to oceanic waves is not generalizable. Further studies with longer simulations and statistical diagnoses (as in Lengaigne et al., 2018; Samson et al., 2014) are necessary to address the physical origin of these differences.

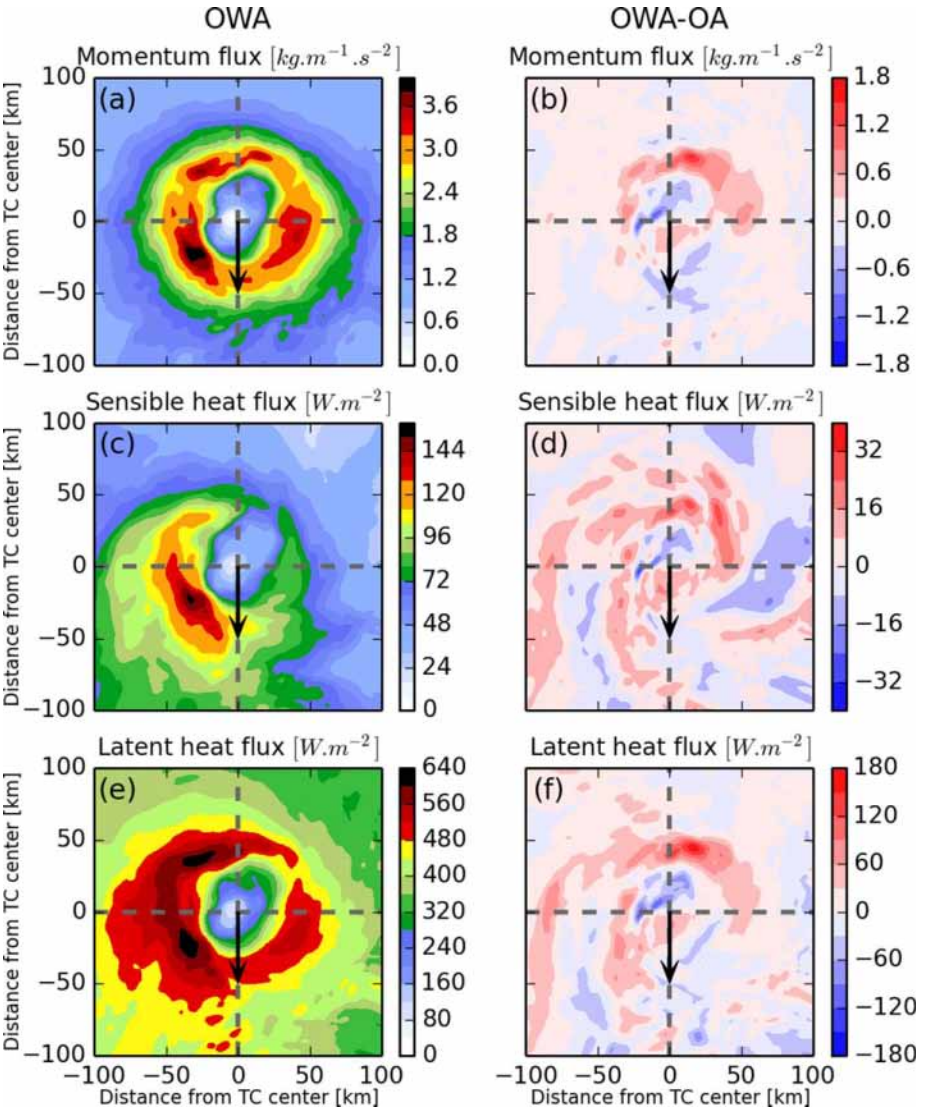

Figure 11. (a) Momentum (kg m^{-1} m^{-2}), (c) sensible heat (W m^{-2}), and (e) latent heat (W m^{-2}) fluxes simulated by the OWA simulation. (b) Differences between OWA and OA simulation for momentum (kg m^{-1} m^{-2}) (d) sensible heat (W m^{-2}), and (f) latent heat (W m^{-2}) fluxes. All these fields are averaged over the simulated time and reoriented along the TC track. The black arrows indicate the direction of TC motion. Gray dashed lines separate the different quadrants of the TC.

6. Impact of the Significant Wave Height on Sea Salt Aerosols

Due to the role of sea salt aerosols in turbulent surface fluxes and their role as cloud condensation nuclei (CCN), the impact of the significant wave height on their emission is analyzed through additional simulations (see Table 1). However as mentioned in section 3.4, the effects of sea salt on turbulent air-sea fluxes and on cloud microphysics are not considered in this paper and will be addressed in a future study.

6.1. Total Sea Salt Aerosol Mass Flux

As discussed previously, oceanic waves are one of the key parameters involved in the sea salt aerosol emissions in high wind conditions. The impact of oceanic waves on the generation of sea salt aerosols is thus examined below. Figures 12a–12f show the net total sea salt flux (sum of emission—dry deposition on the five sea salt aerosol modes) at 06 UTC on 2 January 2014. The only difference between all the simulations is the significant wave height used in the sea salt aerosol source function modeled by the Ovadnevaite et al. (2014) parameterization (see Table 1).

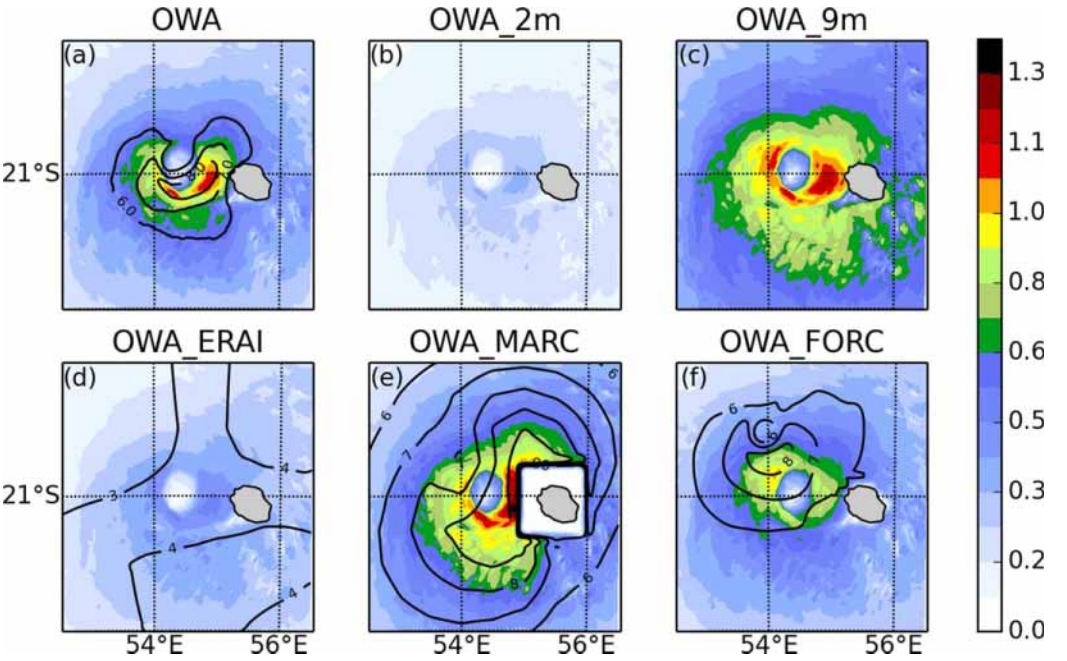

Figure 12. Total instantaneous net sea salt aerosol flux (μg m^{-2} s^{-1}, colors) at 06 UTC on 2 January for the (a) OWA, (b) OWA_2m, (c) OWA_9m, (d) OWA_ERAI, (e) OWA_MARC, and (f) OWA_FORC simulations. Black contours on plot (d) correspond to the 3.0, 3.5, and 4.0 m isolines for the significant wave height from ERA-Interim. Black contours on plots (a), (e), and (f) correspond to the 6, 7, 8, and 9 m isolines for the significant wave height from WW3 online, MARC, and WW3 offline, respectively.

In the OWA simulation (Figure 12a), the highest values of the total net sea salt flux are collocated with the maximum surface wind speed (Figure 5c) and the highest waves (Figure 12a). They reach 1.1 μg m^{-2} s^{-1} in the front quadrants of the eyewall. Along the track of the cyclone, up to 0.8 mg m^{-2} of sea salt aerosols are emitted during the first 36 h (not shown here). Outside the inner core region of the system ($\sim$ 200 km away from the storm center), the total sea salt flux is low (less than 0.3 μg m^{-2} s^{-1}) due to both lower wind speed and lower significant wave height.

The significant wave height used in OWA_2m (Figure 12b) and OWA_9m (Figure 12c) is homogeneous and, thus, does not exhibit the signature of the tropical cyclone. Consequently, the effect of the spatial variation of the significant wave height on sea salt aerosol flux can be examined. As mentioned in section 3.5, 2 and 9 m correspond to the minimum and maximum H_s values encountered in the simulation domain during Bejisa. The asymmetry in the total instantaneous net sea salt aerosol flux is almost lost in these two configurations. Indeed, for both simulations, the maximum sea salt aerosol flux is mainly driven by the 10 m wind speed. Consequently, it is localized in the eastern, southern, and western regions, whereas it was located in the front quadrants of the eyewall in the OWA simulation. Furthermore, the radial gradient of sea salt aerosol fluxes is lower in the OWA_2m and OWA_9m simulations compared to the OWA simulation.

The significant wave height in OWA_ERAI (black contours in Figure 12d) does not show the signature of the tropical cyclone, whereas the OWA, OWA_MARC, and OWA_FORC simulations do (black contours in Figures 12a, 12e, and 12f). H_s is almost uniform all around the cyclone. It only reaches 3–3.5 m while it exceeds 8 m in the OWA simulation. Consequently, the sea salt aerosol flux is around 0.3 μg m^{-2} s^{-1} in the eyewall and barely reaches 0.5 μg m^{-2} s^{-1} on the southern side of the system, where the maximum wind speed is encountered. These values are 2–3 times lower than those of the OWA simulation, which also corresponds to the H_s ratio between the two simulations. The low resolution of ERA-Interim data ($\sim$ 80 km) is mainly responsible for these differences.

The spatial extension of H_s in the OWA_MARC simulation (black contours in Figure 12e) is not consistent with the 10 m wind speed simulated by the OWA simulation (Figure 5c). The maximum of H_s is located in the front quadrants of the TC, where the maximum wind speed is found, while in OWA_MARC, the H_s is

Table 3
Instantaneous Net Sea Salt Aerosol Flux Spatially Averaged Over the Box Displayed in Figure 12 for Each of the Five Modes. ($\mu g\ m^{-2}\ s^{-1}$ and $\#\ m^{-2}\ s^{-1}$)

Simulation Unit	OWA		OWA_2m	OWA_9m
	$\mu g\ m^{-2}\ s^{-1}$ (%)	$\#\ m^{-2}\ s^{-1}$ (%)	$\#\ m^{-2}\ s^{-1}$ (%)	$\#\ m^{-2}\ s^{-1}$ (%)
Mode 1	$7. \times 10^{-4}$ (< 0.5)	6.7×10^{7} (52.5)	3.9×10^{7} (58.7)	9.1×10^{7} (49.5)
Mode 2	1.2×10^{-4} (< 0.5)	6.9×10^{5} (0.5)	2.2×10^{5} (0.3)	1.2×10^{6} (0.6)
Mode 3	5.9×10^{-6} (< 0.5)	$4. \times 10^{3}$ (< 0.01)	2.3×10^{3} (< 0.01)	5.6×10^{3} (< 0.01)
Mode 4	1.9 (99.5)	$6. \times 10^{7}$ (47.0)	2.7×10^{7} (40.9)	9.1×10^{7} (49.5)
Mode 5	9.6×10^{-3} (< 0.5)	2.7×10^{3} (< 0.01)	1.1×10^{3} (< 0.01)	4.3×10^{3} (< 0.01)

Note. For the OWA Simulation, Both the Mass Flux ($\mu g\ m^{-2}\ s^{-1}$) and the Number Flux ($\#\ m^{-2}\ s^{-1}$) are Displayed. For the OWA_2m and OWA_9m Simulations the Net Sea Salt Aerosol Flux is Presented. In parenthesis is the contribution of each mode to the total flux (in percentage).

homogeneous over the TC. This is explained by the low resolution of the wave model used in the MARC database (0.5°). These H_s differences imply strong differences in the instantaneous net sea salt fluxes, which are higher by a factor of 1.5 in the OWA_MARC simulation (Figure 12e) than in the OWA simulation (Figure 12a).

The OWA_FORC simulation highlights the problem of using a wave field from a model where the storm has a different position. Since the OWA_FORC simulation uses the H_s from WW3 forced by the ECMWF operational high-resolution analysis (black contours in Figure 12f), the significant wave height is consistent with the wind field of the ECMWF analysis and not with that of the Meso-NH simulation. In the ECMWF analysis, the center of the cyclone is located ∼50–60 km north-west of its actual position in the OWA simulation. Since the significant wave height has maximum values (∼8 m) north of the position of the simulated cyclone, the net sea salt aerosol flux is enhanced in the northern part of the cyclone (Figure 12f). Thus, the net sea salt flux reaches 0.9 $\mu g\ m^{-2}\ s^{-1}$ in the north-west quadrant while it only reaches 0.6 $\mu g\ m^{-2}\ s^{-1}$ in the southern quadrant, introducing strong asymmetry in the sea salt aerosol emissions due to inconsistent significant wave height.

Using the sea state from a full ocean-waves-atmosphere coupled system is essential to obtain consistent sea salt emissions. It produces asymmetric sea salt emissions by collocating the maximum of the sea salt flux with the highest values of surface wind speed and significant wave height. This will be a key point when considering the effect of sea salt on momentum and heat fluxes, and on the cloud lifecycle.

6.2. Modal Net Sea Salt Aerosol Mass and Number Fluxes

Table 3 presents the impact of different significant wave height on the modal distribution of the instantaneous net sea salt aerosol fluxes (emission–dry deposition for the five sea salt aerosol modes) for OWA, OWA_2m, and OWA_9m simulations (see Table 1). As mentioned in section 3.1, the sea salt aerosols distributions are modeled by five log-normal modes, ranging from ultrafine sea salt aerosols (nm) to coarse ones (μm).

For the OWA simulation, the sea salt aerosol mass flux is maximum for the fourth mode and reaches 1.9 $\mu g\ m^{-2}\ s^{-1}$. This is the main contribution (99.5%) to the total net sea salt aerosol mass flux (Figure 12). The sea salt aerosol mass flux in the four other modes is $\sim 10^2$ (fifth mode) to 10^6 times (third mode) less important than in the fourth mode. From a microphysical point of view, it is interesting to look at the sea salt aerosol flux in terms of number concentration. The highest net sea salt aerosol number flux occurs for modes 1 and 4 with about 6.0×10^7 particles $m^{-2}\ s^{-1}$ emitted for the OWA simulation. About $\sim 10^2$ and $\sim 10^4$ times less particles are emitted in the second mode, and in the third and fifth mode, respectively. It must be noted that the larger sea salt particles can more readily act as CCN because they require smaller supersaturations to be activated to become a cloud droplet (Seinfeld & Pandis, 2016).

When a constant and homogeneous significant wave height of 2 m (OWA_2m) is imposed (it corresponds to a wave height encountered more than 500 km away from the tropical cyclone center), the sea salt aerosol number flux in the fourth mode is theoretically decreased compared to the OWA simulation (Table 3). However, it is important to note that the contribution of the fourth mode to the total number flux has

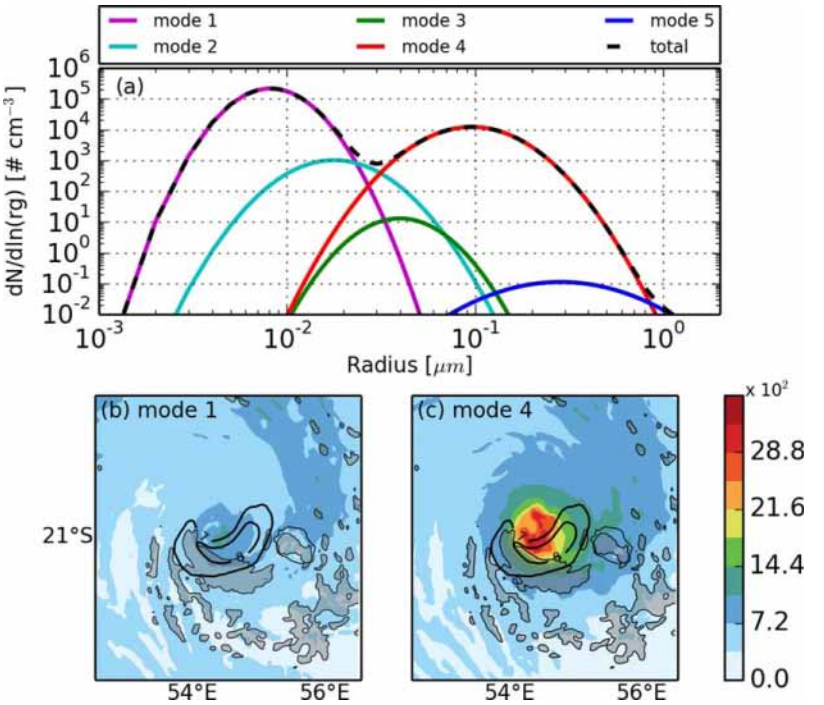

Figure 13. (a) Sea salt aerosol number size distribution for the OWA simulation. Number concentration of sea salt aerosols vertically averaged from the ground to the altitude of the isotherm 0°C (# cm^{-3}) for the (b) first and (c) fourth modes in the OWA simulation. Black contours on (b) and (c) correspond to H_s values of 7 and 8 m. The gray shaded areas correspond to instantaneous rain rate higher than 10 mm h^{-1}.

decreased from 47.0 to 40.9%, while the contribution of the first mode has increased from 52.5 to 58.8%. The second, third, and fifth modes contribute to less than 1% to the total number flux. In the OWA_9m simulation, a H_s value of 9 m, which is almost the maximum value simulated in the inner core of the system, is imposed over the domain. The first and fourth modes have the same contribution to the total number flux ($\sim$9.1 $\times$ 10^7 particles m^{-2} $^{-1}$). Contrary to the OWA_2m simulation, the contribution of the fourth mode has increased (from 47.0 to 49.5%) while the one of the first mode has decreased (from 52.5 to 49.5%). Consequently, the significant wave height does not only impact the amount of particles emitted at the ocean surface, but it also influences the proportion of aerosol particles in the five modes which is a key point for cloud droplets generation.

Figure 13a shows the sea salt aerosol number size distribution for the OWA simulation. It clearly shows that the first and fourth modes are the most important modes in terms of number concentration. The spatial variation of the sea salt aerosol number concentration integrated from 0 m to the altitude of the isotherm 0°C is plotted in Figures 13b and 13c for these two modes in the OWA simulation. In the rainband located north-east of the tropical cyclone center, the number concentration is similar for the two modes ($\sim$1,100 particles cm^{-3}). The precipitation in this region is relatively scarce, and aerosols are not efficiently scavenged. In the inner core of the system, the particles number of the two modes is very different. While it reaches 3,000 particles cm^{-3} in the fourth mode, it does not exceeds 1,500 particles cm^{-3} in the first mode. This difference can be attributed to the sea salt aerosol scavenging that acts differently in the two modes. Aerosol scavenging is less efficient for aerosol particles with radius between 0.1 and 1 μm (Randerson, 1984). Therefore, sea salt aerosols in this range of radius (typically mode 5 and part of mode 4; see Figure 13a) are still available in the atmosphere.

It is evident from these results that a careful description of the significant wave height can affect not only the spatial distribution of sea salt aerosols, but also the relative contribution of each mode in the total number flux. The number of particles in each mode is crucial for an integration in aerosols and microphysics schemes since these physical processes are strongly size-dependent.

7. Conclusions

A newly developed Ocean-Waves-Atmosphere coupled system called MSWC for Meso-NH/SurfEx/WW3/CROCO is presented in this paper. For the first time, MSWC is used to simulate a tropical cyclone. The case study is Tropical Cyclone Bejisa, which passed close to La Réunion in January 2014. The effects of the oceanic waves on the ocean and the atmosphere are examined. Through five numerical experiments, attention is focused on the impact of the oceanic waves on different surface parameters such as the Charnock parameter, the roughness length, the turbulent fluxes, and the sea salt aerosol emissions.

Overall, the ability of the fully coupled system to reproduce the behavior of the OWA interactions in the context of a tropical cyclone has been shown. The track of Bejisa was well reproduced by the model. The trend of the intensity was fairly well simulated, but its amplitude was underestimated compared to the best-track analysis. The significant wave height from the wave model exhibits a bean-like structure with the maximum values in the front quadrants of the tropical cyclone. This structure is produced by the higher wind speed in those quadrants associated with the forward motion of the storm. These quadrants are thus associated with an increase of the effective fetch in the direction of the motion of the storm. The simulated significant wave height shows globally good agreement with buoy and altimeter measurements available during this time period. The well-known decrease of the sea surface temperature in the wake of the tropical cyclone is also simulated with an increase of the depth of the thermocline. After the passage of Bejisa, a rising of the thermocline is visible. In addition, an inertial oscillation is simulated behind the tropical cyclone with a period of approximately 1 day.

The impact of oceanic waves on turbulent surface fluxes is mitigated despite a small increase of the momentum and heat fluxes when coupling with a wave model. Further studies are necessary to address the physical origin of this difference. The spatial distribution and magnitude of the sea salt aerosol fluxes and concentration of each mode show a strong dependence on the significant wave height field. It has been shown that online coupling of a wave model and an atmospheric model is necessary if the aim is to simulate sea salt aerosol emissions consistent with the wind and wave fields that generate them. Forced systems mainly have sea salt aerosol fluxes that are not located where the maximum wave heights are present. High-resolution wave height forced by another meteorological model tends to locate the sea salt source in the wrong region while low-resolution wave height data does not reproduce the magnitude of the emission. The correct location of the sea salt sources is a key point when considering the impact of sea salt on the heat and momentum fluxes. It will also be of major importance when using the sea salt aerosols generated by the cyclonic winds and waves as a source of cloud condensation and ice freezing nuclei in multimoment microphysical schemes. The complex 3-D structure of the ocean and the atmosphere and the very localized position of the oceanic waves in the front of the eyewall structure impose the use of a fully coupled system to study the turbulent and sea salt aerosol fluxes.

Tropical Cyclone Bejisa was chosen as a case study because it passed close to La Réunion, where some observations were available. In addition, high-resolution AROME-IO analyses were available which avoided the need to use a bogus or a long spin-up period. More case studies are now required to draw more general conclusions about the effect of oceanic waves on atmospheric and oceanic parameters. Such a high-resolution, fully coupled model could be used for a large panel of applications. The air-sea interactions during intensification stages could be studied and additional parameterizations of the air-sea exchanges should be tested. This model is also a powerful tool to analyze the sea state and wind field during extreme weather events, in particular for dimensioning the technology for renewable marine energy in cyclonic basins.

Acknowledgments
This work was carried out in the framework of the DiMe project, which benefits from government support managed by the Agence Nationale de la Recherche under the Investissement d'Avenir program with the reference ANR-10-IEED-0006–14. Additional financial support was also provided by the Université de la Réunion through the federation Observatoire des Milieux Naturels et des Changements Globaux (OMNCG) of the Observatoire des Sciences de l'Univers de la Réunion (OSU-R). Thanks to the reviewers for their suggestions and comments that helped to improve the manuscript. We are grateful to the society NortekMed and the DDE (Direction Départementale de l'Equipement) for providing buoy data. Philippe Caroff and Sébastien Langlade (Météo-France/RSMC La Réunion) are acknowledged for their detailed report about Bejisa cyclogenesis and evolution. Françoise Orain, Stéphane Saux-Picart, and Marie-Noelle Bouin are also acknowledged for their discussions of sea surface temperature data and turbulent surface fluxes parameterization. The simulations were performed on the supercomputer "beaufix" of Météo-France in Toulouse, France. The models used in this paper are open-source and available freely at the following websites: http://mesonh.aero.obs-mip.fr for Meso-NH/SurfEx, https://gforge.inria.fr/projects/croco/ for CROCO, https://forge.ifremer.fr/svn/ww3 for WW3, and https://portal.enes.org/oasis for OASIS.

References

Aijaz, S., Ghantous, M., Babanin, A. V., Ginis, I., Thomas, B., & Wake, G. (2017). Nonbreaking wave-induced mixing in upper ocean during tropical cyclones using coupled hurricane-ocean-wave modeling. *Journal of Geophysical Research: Oceans*, *122*, 3939–3963. https://doi.org/10.1002/2016JC012219

Andreas, E. L. (2004). Spray stress revisited. *Journal of Physical Oceanography*, *34*(6), 1429–1440. https://doi.org/10.1175/1520-0485(2004)034<1429:SSR>2.0.CO;2

Andreas, E. L., & Emanuel, K. A. (2001). Effects of sea spray on tropical cyclone intensity. *Journal of the Atmospheric Sciences*, *58*(24), 3741–3751. https://doi.org/10.1175/1520-0469(2001)058<3741:EOSSOT>2.0.CO;2

Ardhuin, F., O'Reilly, W. C., Herbers, T. H. C., & Jessen, P. F. (2003). Swell transformation across the continental shelf. Part I: Attenuation and directional broadening. *Journal of Physical Oceanography*, *33*(9), 1921–1939. https://doi.org/10.1175/1520-0485(2003)033<1921:STATCS>2.0.CO;2

Ardhuin, F., Rogers, E., Babanin, A. V., Filipot, J.-F., Magne, R., Roland, A., et al. (2010). Semiempirical dissipation source functions for ocean waves. Part I: Definition, calibration, and validation. *Journal of Physical Oceanography*, *40*(9), 1917–1941. https://doi.org/10.1175/2010JPO4324.1

Ardhuin, F., & Roland, A. (2012). Coastal wave reflection, directional spread, and seismoacoustic noise sources. *Journal of Geophysical Research*, *117*, C00J20. https://doi.org/10.1029/2011JC007832

Bao, J.-W., Wilczak, J. M., Choi, J.-K., & Kantha, L. H. (2000). Numerical simulations of air-sea interaction under high wind conditions using a coupled model: A study of hurricane development. *Monthly Weather Review*, *128*(7), 2190–2210. https://doi.org/10.1175/1520-0493(2000)128<2190:NSOASI>2.0.CO;2

Barthe, C., Hoarau, T., & Bovalo, C. (2016). Cloud electrification and lightning activity in a tropical cyclone-like vortex. *Atmospheric Research*, *180*, 297–309. https://doi.org/10.1016/j.atmosres.2016.05.023

Battjes, J. A., & Janssen, J. P. F. M. (1978). Energy loss and set-up due to breaking of random waves. In *Coastal engineering 1978* (pp. 569–587). New York, NY: American Society of Civil Engineers. https://doi.org/10.1061/9780872621909.034

Bechtold, P., Bazile, E., Guichard, F., Mascart, P., & Richard, E. (2001). A mass-flux convection scheme for regional and global models. *Quarterly Journal of the Royal Meteorological Society*, *127*, 869–886.

Beckmann, A., & Haidvogel, D. B. (1993). Numerical simulation of flow around a tall isolated seamount. Part I: Problem formulation and model accuracy. *Journal of Physical Oceanography*, *23*(8), 1736–1753. https://doi.org/10.1175/1520-0485(1993)023<1736:NSOFAA>2.0.CO;2

Bender, M. A., & Ginis, I. (2000). Real-case simulations of hurricane-ocean interaction using a high-resolution coupled model: Effects on hurricane intensity. *Monthly Weather Review*, *128*(4), 917–946. https://doi.org/10.1175/1520-0493(2000)128<0917:RCSOHO>2.0.CO;2

Berrisford, P., Dee, D., Poli, P., Brugge, P., Fielding, R., Fuentes, K. M., et al. (2011). *The ERA-Interim archive version 2.0* (ERA Rep. Ser. 1). Reading, UK: European Centre for Medium-Range Weather Forecasts (ECMWF).

Bougeault, P., & Lacarrère, P. (1989). Parameterization of orography-induced turbulence in a mesobeta-scale model. *Monthly Weather Review*, *117*(8), 1872–1890. https://doi.org/10.1175/1520-0493(1989)117<1872:POOITI>2.0.CO;2

Breivik, Ø., Mogensen, K., Bidlot, J.-R., Balmaseda, M. A., & Janssen, P. A. E. M. (2015). Surface wave effects in the NEMO ocean model: Forced and coupled experiments. *Journal of Geophysical Research: Oceans*, *120*, 2973–2992. https://doi.org/10.1002/2014JC010565

Chane-Ming, F., Ibrahim, C., Barthe, C., Jolivet, S., Keckhut, P., Liou, Y.-A., et al. (2014). Observation and a numerical study of gravity waves during tropical cyclone Ivan (2008). *Atmospheric Chemistry and Physics*, *14*(2), 641–658. https://doi.org/10.5194/acp-14-641-2014

Charnock, H. (1955). Wind stress on a water surface. *Quarterly Journal of the Royal Meteorological Society*, *81*(350), 639–640. https://doi.org/10.1002/qj.49708135027

Chen, S. S., & Curcic, M. (2016). Ocean surface waves in Hurricane Ike (2008) and Superstorm Sandy (2012): Coupled model predictions and observations. *Ocean Modelling*, *103*, 161–176. https://doi.org/10.1016/j.ocemod.2015.08.005

Chen, S. S., Zhao, W., Donelan, M. A., Price, J. F., & Walsh, E. J. (2007). The CBLAST-hurricane program and the next-generation fully coupled atmosphere-wave-ocean models for hurricane research and prediction. *Bulletin of the American Meteorological Society*, *88*(3), 311–317. https://doi.org/10.1175/BAMS-88-3-311

Claeys, M. (2016). *Modélisation des aérosols marins et de leur impact radiatif direct sur le bassin méditerranéen dans le cadre du projet CHARMEX* (Ph.D. thesis). Toulouse, France: Université de Toulouse.

Cline, I. M. (1920). Relation of changes in storm tides on the coast of the Gulf of Mexico to the center and movement of hurricanes. *Monthly Weather Review*, *48*(3), 127–146. https://doi.org/10.1175/1520-0493(1920)48<127:ROCIST>2.0.CO;2

Colella, P., & Woodward, P. R. (1984). The piecewise parabolic method (PPM) for gas-dynamical simulations. *Journal of Computational Physics*, *54*(1), 174–201. https://doi.org/10.1016/0021-9991(84)90143-8

Craig, A., Valcke, S., & Coquart, L. (2017). Development and performance of a new version of the OASIS coupler, OASIS3-MCT_3.0. *Geoscientific Model Development*, *10*, 3297–3308. https://doi.org/10.5194/gmd-10-3297-2017

Cuxart, J., Bougeault, P., & Redelsperger, J.-L. (2000). A turbulence scheme allowing for mesoscale and large-eddy simulations. *Quarterly Journal of the Royal Meteorological Society*, *126*, 1–30.

D'Asaro, E. A., Sanford, T. B., Niiler, P. P., & Terrill, E. J. (2007). Cold wake of hurricane Frances. *Geophysical Research Letters*, *34*, L15609. https://doi.org/10.1029/2007GL030160

Davy, C., Barruol, G., Fontaine, F., & Cordier, E. (2016). Analyses of extreme swell events on La Réunion Island from microseismic noise. *Geophysical Journal International*, *207*(3), 1767–1782. https://doi.org/10.1093/gji/ggw365

Debreu, L., Marchesiello, P., Penven, P., & Cambon, G. (2012). Two-way nesting in split-explicit ocean models: Algorithms, implementation and validation. *Ocean Modelling*, *49–50*, 1–21. https://doi.org/10.1016/j.ocemod.2012.03.003

de Leeuw, G., Andreas, E. L., Anguelova, M. D., Fairall, C. W., Lewis, E. R., O'Dowd, C., et al. (2011). Production flux of sea spray aerosol. *Reviews of Geophysics*, *49*, RG2001. https://doi.org/10.1029/2010RG000349

DeMott, P. J., Hill, T. C. J., McCluskey, C. S., Prather, K. A., Collins, D. B., Sullivan, R. C., et al. (2016). Sea spray aerosol as a unique source of ice nucleating particles. *Proceedings of the National Academy of Sciences of the United States of America*, *113*(21), 5797–5803. https://doi.org/10.1073/pnas.1514034112

Doyle, J. D. (2002). Coupled atmosphere-ocean wave simulations under high wind conditions. *Monthly Weather Review*, *130*(12), 3087–3099. https://doi.org/10.1175/1520-0493(2002)130<3087:CAOWSU>2.0.CO;2

Doyle, J. D., Hodur, R., Chen, S., Jin, Y., Msokaitis, J., Wang, S., et al. (2014). Tropical cyclone prediction using COAMPS-TC. *Oceanography*, *27*(3), 104–115. https://doi.org/10.5670/oceanog.2014.72

Emanuel, K. A. (1986). An air-sea interaction theory for tropical cyclones. Part I: Steady-state maintenance. *Journal of the Atmospheric Sciences*, *43*(6), 585–605. https://doi.org/10.1175/1520-0469(1986)043<0585:AASITF>2.0.CO;2

Esquivel-Trava, B., Ocampo-Torres, F. J., & Osuna, P. (2015). Spatial structure of directional wave spectra in hurricanes. *Ocean Dynamics*, *65*(1), 65–76. https://doi.org/10.1007/s10236-014-0791-9

Fairall, C. W., Bradley, E. F., Hare, J. E., Grachev, A. A., & Edson, J. B. (2003). Bulk parameterization of air-sea fluxes: Updates and verification for the COARE algorithm. *Journal of Climate*, *16*(4), 571–591. https://doi.org/10.1175/1520-0442(2003)016<0571:BPOASF>2.0.CO;2

Fairall, C. W., Kepert, J. D., & Holland, G. J. (1994). The effect of sea spray on surface energy transports over the ocean. *Global Atmosphere and Ocean System*, *2*(2–3), 121–142.

Fan, J., Wang, Y., Rosenfeld, D., & Liu, X. (2016). Review of aerosol-cloud interactions: Mechanisms, significance, and challenges. *Journal of the Atmospheric Sciences*, *73*(11), 4221–4252. https://doi.org/10.1175/JAS-D-16-0037.1

Fierro, A. O., Rogers, R. F., Marks, F. D., & Nolan, D. S. (2009). The impact of horizontal grid spacing on the microphysical and kinematic structures of strong tropical cyclones simulated with the WRF-ARW model. *Monthly Weather Review*, *137*(11), 3717–3743. https://doi.org/10.1175/2009MWR2946.1

Gentry, M. S., & Lackmann, G. M. (2010). Sensitivity of simulated tropical cyclone structure and intensity to horizontal resolution. *Monthly Weather Review*, *138*(3), 688–704. https://doi.org/10.1175/2009MWR2976.1

Gregory, D., Morcrette, J.-J., Jakob, C., Beljaars, A. C. M., & Stockdale, T. (2010). Revision of convection, radiation and cloud schemes in the ECMWF integrated forecasting system. *Quarterly Journal of the Royal Meteorological Society*, *126*(566), 1685–1710. https://doi.org/10.1002/qj.49712656607

Grythe, H., Ström, J., Krejci, R., Quinn, P., & Stohl, A. (2014). A review of sea-spray aerosol source functions using a large global set of sea salt aerosol concentration measurements. *Atmospheric Chemistry and Physics*, *14*(3), 1277–1297. https://doi.org/10.5194/acp-14-1277-2014

Hare, J. E., Persson, P. O. G., Fairall, C., & Edson, J. (1999). Behavior of Charnock's relationship for high wind conditions. In *Proceedings of 13th Symposium of Boundary Layers and Turbulence* (pp. 252–255). Dallas, TX: American Meteorological Society.

Hasselmann, S., Hasselmann, K., Allender, J. H., & Barnett, T. P. (1985). Computations and parameterizations of the nonlinear energy transfer in a gravity-wave spectrum. Part II: Parameterizations of the nonlinear energy transfer for application in wave models. *Journal of Physical Oceanography*, *15*(11), 1378–1391. https://doi.org/10.1175/1520-0485(1985)015<1378:CAPOTN>2.0.CO;2

Herbener, S. R., van den Heever, S. C., Carrió, G. G., Saleeby, S. M., & Cotton, W. R. (2014). Aerosol indirect effects on idealized tropical cyclone dynamics. *Journal of the Atmospheric Sciences*, *71*(6), 2040–2055. https://doi.org/10.1175/JAS-D-13-0202.1

Holland, G. J. (1997). The maximum potential intensity of tropical cyclones. *Journal of the Atmospheric Sciences*, *54*(21), 2519–2541. https://doi.org/10.1175/1520-0469(1997)054<2519:TMPIOT>2.0.CO;2

Jacob, R., Larson, J., & Ong, E. (2005). M × N communication and parallel interpolation in community climate system model version 3 using the model coupling toolkit. *International Journal of High Performance Computing Applications*, *19*(3), 293–307. https://doi.org/10.1177/1094342005056116

Jaeglé, L., Quinn, P. K., Bates, T. S., Alexander, B., & Lin, J.-T. (2011). Global distribution of sea salt aerosols: New constraints from in situ and remote sensing observations. *Atmospheric Chemistry and Physics*, *11*(7), 3137–3157. https://doi.org/10.5194/acp-11-3137-2011

Janssen, P. A. E. M. (1991). Quasi-linear theory of wind-wave generation applied to wave forecasting. *Journal of Physical Oceanography*, *21*(11), 1631–1642. https://doi.org/10.1175/1520-0485(1991)021<1631:QLTOWW>2.0.CO;2

Jin, H., Peng, M. S., Jin, Y., & Doyle, J. D. (2014). An evaluation of the impact of horizontal resolution on tropical cyclone predictions using COAMPS-TC. *Weather and Forecasting*, *29*(2), 252–270. https://doi.org/10.1175/WAF-D-13-00054.1

Jolivet, S., Chane-Ming, F., Barbary, D., & Roux, F. (2013). A numerical study of orographic forcing on TC Dina (2002) in South West Indian Ocean. *Annales Geophysicae*, *31*(1), 107–125. https://doi.org/10.5194/angeo-31-107-2013

Jones, P. W. (1999). First- and second-order conservative remapping schemes for grids in spherical coordinates. *Monthly Weather Review*, *127*(9), 2204–2210. https://doi.org/10.1175/1520-0493(1999)127<2204:FASOCR>2.0.CO;2

Jullien, S., Marchesiello, P., Menkes, C. E., Lefèvre, J., Jourdain, N. C., Samson, G., et al. (2014). Ocean feedback to tropical cyclones: Climatology and processes. *Climate Dynamics*, *43*(9–10), 2831–2854. https://doi.org/10.1007/s00382-014-2096-6

Jullien, S., Menkes, C. E., Marchesiello, P., Jourdain, N. C., Lengaigne, M., Koch-Larrouy, A., et al. (2012). Impact of tropical cyclones on the heat budget of the South Pacific Ocean. *Journal of Physical Oceanography*, *42*(11), 1882–1906. https://doi.org/10.1175/JPO-D-11-0133.1

Kaplan, J., DeMaria, M., & Knaff, J. A. (2010). A revised tropical cyclone rapid intensification index for the Atlantic and Eastern North Pacific basins. *Weather and Forecasting*, *25*(1), 220–241. https://doi.org/10.1175/2009WAF2222280.1

Kudryavtsev, V. N., & Makin, V. K. (2007). Aerodynamic roughness of the sea surface at high winds. *Boundary-Layer Meteorology*, *125*(2), 289–303. https://doi.org/10.1007/s10546-007-9184-7

Large, W. G., McWilliams, J. C., & Doney, S. C. (1994). Oceanic vertical mixing: A review and a model with a nonlocal boundary layer parameterization. *Reviews of Geophysics*, *32*(4), 363–403. https://doi.org/10.1029/94RG01872

Larson, J., Jacob, R., & Ong, E. (2005). The model coupling toolkit: A new Fortran90 toolkit for building multiphysics parallel coupled models. *International Journal of High Performance Computing Applications*, *19*(3), 277–292. https://doi.org/10.1177/1094342005056115

Lebeaupin Brossier, C., Ducrocq, V., & Giordani, H. (2008). Sensitivity of three Mediterranean heavy rain events to two different sea surface fluxes parameterizations in high-resolution numerical modeling. *Journal of Geophysical Research*, *113*, D21109. https://doi.org/10.1029/2007JD009613

Lee, C.-Y., & Chen, S. S. (2012). Symmetric and asymmetric structures of hurricane boundary layer in coupled atmosphere-wave-ocean models and observations. *Journal of the Atmospheric Sciences*, *69*(12), 3576–3594. https://doi.org/10.1175/JAS-D-12-046.1

Lee, C.-Y., & Chen, S. S. (2014). Stable boundary layer and its impact on tropical cyclone structure in a coupled atmosphere-ocean model. *Monthly Weather Review*, *142*(5), 1927–1944. https://doi.org/10.1175/MWR-D-13-00122.1

Lenain, L., & Melville, W. K. (2017). Evidence of sea-state dependence of aerosol concentration in the marine atmospheric boundary layer. *Journal of Physical Oceanography*, *47*(1), 69–84. https://doi.org/10.1175/JPO-D-16-0058.1

Lengaigne, M., Neetu, S., Samson, G., Vialard, J., Krishnamohan, K. S., Masson, S., et al. (2018). Influence of air-sea coupling on Indian Ocean tropical cyclones. *Climate Dynamics*, https://doi.org/10.1007/s00382-018-4152-0, in press.

Lionello, P., Malguzzi, P., & Buzzi, A. (1998). Coupling between the atmospheric circulation and the ocean wave field: An idealized case. *Journal of Physical Oceanography*, *28*(2), 161–177. https://doi.org/10.1175/1520-0485(1998)028<0161:CBTACA>2.0.CO;2

Liu, B., Guan, C., Xie, L., & Zhao, D. (2012). An investigation of the effects of wave state and sea spray on an idealized typhoon using an air-sea coupled modeling system. *Advances in Atmospheric Sciences*, *29*(2), 391–406. https://doi.org/10.1007/s00376-011-1059-7

Liu, B., Liu, H., Xie, L., Guan, C., & Zhao, D. (2011). A coupled atmosphere-wave-ocean modeling system: Simulation of the intensity of an idealized tropical cyclone. *Monthly Weather Review*, *139*(1), 132–152. https://doi.org/10.1175/2010MWR3396.1

Marchesiello, P., Benshila, R., Almar, R., Uchiyama, Y., McWilliams, J. C., & Shchepetkin, A. (2015). On tridimensional rip current modeling. *Ocean Modelling*, *96*, 36–48. https://doi.org/10.1016/j.ocemod.2015.07.003

Masson, V., Le Moigne, P., Martin, E., Faroux, S., Alias, A., Alkama, R., et al. (2013). The SURFEXv7.2 land and ocean surface platform for coupled or offline simulation of earth surface variables and fluxes. *Geoscientific Model Development*, *6*(4), 929–960. https://doi.org/10.5194/gmd-6-929-2013

McCluskey, C. S., Hill, T. C. J., Malfatti, F., Sultana, C. M., Lee, C., Santander, M. V., et al. (2017). A dynamic link between ice nucleating particles released in nascent sea spray aerosol and oceanic biological activity during two mesocosm experiments. *Journal of the Atmospheric Sciences*, *74*(1), 151–166. https://doi.org/10.1175/JAS-D-16-0087.1

Menemenlis, D., Campin, J., Heimbach, P., Hill, C., Lee, T., Nguyen, A., et al. (2008). ECCO2: High resolution global ocean and sea ice data synthesis. *Eos, Transactions American Geophysical Union*, *89*(53), Fall Meeting Supplement, Abstract OS31C-1292.

Mlawer, E. J., Taubman, S. J., Brown, P. D., Iacono, M. J., & Clough, S. A. (1997). Radiative transfer for inhomogeneous atmospheres: RRTM, a validated correlated-k model for the longwave. *Journal of Geophysical Research*, *102*(D14), 16663–16682. https://doi.org/10.1029/97JD00237

Monahan, E. C., Spiel, D. E., & Davidson, K. L. (1986). *A model of marine aerosol generation via whitecaps and wave disruption* (pp. 167–174). Dordrecht, the Netherlands: Springer. https://doi.org/10.1007/978-94-009-4668-2_16

Moon, I.-J., Ginis, I., Hara, T., & Thomas, B. (2007). A physics-based parameterization of air-sea momentum flux at high wind speeds and its impact on hurricane intensity predictions. *Monthly Weather Review*, *135*(8), 2869–2878. https://doi.org/10.1175/MWR3432.1

Moon, I.-J., Ginis, I., Hara, T., Tolman, H. L., Wright, C. W., & Walsh, E. J. (2003). Numerical simulation of sea surface directional wave spectra under hurricane wind forcing. *Journal of Physical Oceanography*, *33*(8), 1680–1706. https://doi.org/10.1175/2410.1

Noilhan, J., & Planton, S. (1989). A simple parametrization of land surface processes for meteorological models. *Monthly Weather Review*, *117*, 536–549.

Nuissier, O., Rogers, R. F., & Roux, F. (2005). A numerical simulation of Hurricane Bret on 22–23 August 1999 initialized with airborne Doppler radar and dropsonde data. *Quarterly Journal of the Royal Meteorological Society*, *131*(605), 155–194. https://doi.org/10.1256/qj.02.233

Ovadnevaite, J., Manders, A., De Leeuw, G., Ceburnis, D., Monahan, C., Partanen, A.-I., et al. (2014). A sea spray aerosol flux parameterization encapsulating wave state. *Atmospheric Chemistry and Physics*, *14*, 1837–1852. https://doi.org/10.5194/acp-14-1837-2014

Pantillon, F. P., Chaboureau, J.-P., Mascart, P. J., & Lac, C. (2013). Predictability of a Mediterranean tropical-like storm downstream of the extratropical transition of hurricane Helene (2006). *Monthly Weather Review*, *141*(6), 1943–1962. https://doi.org/10.1175/MWR-D-12-00164.1

Pantillon, F., Chaboureau, J.-P., & Richard, E. (2015). Remote impact of North Atlantic hurricanes on the Mediterranean during episodes of intense rainfall in autumn 2012. *Quarterly Journal of the Royal Meteorological Society*, *141*(688), 967–978. https://doi.org/10.1002/qj.2419

Pantillon, F., Chaboureau, J.-P., & Richard, E. (2016). Vortex-vortex interaction between Hurricane Nadine (2012) and an Atlantic cut-off dropping the predictability over the Mediterranean. *Quarterly Journal of the Royal Meteorological Society*, *142*(S1), 419–432. https://doi.org/10.1002/qj.2635

Penven, P., Debreu, L., Marchesiello, P., & McWilliams, J. C. (2006). Evaluation and application of the ROMS 1-way embedding procedure to the central California upwelling system. *Ocean Modelling*, *12*(1–2), 157–187. https://doi.org/10.1016/j.ocemod.2005.05.002

Pinty, J.-P., & Jabouille, P. (1998). *A mixed-phase cloud parameterization for use in a mesoscale non-hydrostatic model: Simulations of a squall line and of orographic precipitation*. In Proceedings of Conference on Cloud Physics (pp. 217–220). Everett, WA: American Meteorological Society.

Potter, H., Collins, C. O., Drennan, W. M., & Graber, H. C. (2015). Observations of wind stress direction during Typhoon Chaba (2010). *Geophysical Research Letters*, *42*, 9898–9905. https://doi.org/10.1002/2015GL065173

Powell, M. D., Vickery, P. J., & Reinhold, T. A. (2003). Reduced drag coefficient for high wind speeds in tropical cyclones. *Nature*, *422*(6929), 279–283. https://doi.org/10.1038/nature01481

Price, J. F. (1981). Upper ocean response to a hurricane. *Journal of Physical Oceanography*, *11*(2), 153–175. https://doi.org/10.1175/1520-0485(1981)011<0153:UORTAH>2.0.CO;2

Queffeulou, P., & Croizé-Fillon, D. (2017). *Global altimeter SWH data set–Version 11.0* (technical report). Plouzané, France: IFREMER.

Randerson, D. (Eds.) (1984). *Atmospheric science and power production* (Tech. Rep. DOE/TIC-27601). Washington, DC: Technical Information Center, Division of Biomedical Environmental Research, U.S. Department of Energy. https://doi.org/10.2172/6503687

Richter, D. H., & Stern, D. P. (2014). Evidence of spray-mediated air-sea enthalpy flux within tropical cyclones. *Geophysical Research Letters*, *41*, 2997–3003. https://doi.org/10.1002/2014GL059746

Rosenfeld, D., Andreae, M. O., Asmi, A., Chin, M., de Leeuw, G., Donovan, D. P., et al. (2014). Global observations of aerosol-cloud-precipitation-climate interactions. *Reviews of Geophysics*, *52*, 750–808. https://doi.org/10.1002/2013RG000441

Rosenfeld, D., Woodley, W. L., Khain, A., Cotton, W. R., Carrió, G., Ginis, I., et al. (2012). Aerosol effects on microstructure and intensity of tropical cyclones. *Bulletin of the American Meteorological Society*, *93*(7), 987–1001. https://doi.org/10.1175/BAMS-D-11-00147.1

Rotunno, R., & Emanuel, K. A. (1987). An air-sea interaction theory for tropical cyclones. Part II: Evolutionary study using a nonhydrostatic axisymmetric numerical model. *Journal of the Atmospheric Sciences*, *44*(3), 542–561. https://doi.org/10.1175/1520-0469(1987)044<0542:AAITFT>2.0.CO;2

Samson, G., Masson, S., Lengaigne, M., Keerthi, M. G., Vialard, J., Pous, S., et al. (2014). The NOW regional coupled model: Application to the tropical Indian Ocean climate and tropical cyclone activity. *Journal of Advances in Modeling Earth Systems*, *6*, 700–722. https://doi.org/10.1002/2014MS000324

Seinfeld, J. H., & Pandis, S. N. (2016). *Atmospheric chemistry and physics: From air pollution to climate change* (1152 p.). Hoboken, NJ: John Wiley & Sons.

Seyfried, L., Marsaleix, P., Richard, E., & Estournel, C. (2017). Modelling deep-water formation in the North-West Mediterranean Sea with a new air-sea coupled model: Sensitivity to turbulent flux parameterizations. *Ocean Science*, *13*, 1093–1112. https://doi.org/10.5194/os-13-1093-2017

Shanas, P., Sanil Kumar, V., & Hithin, N. (2014). Comparison of gridded multi-mission and along-track mono-mission satellite altimetry wave heights with in situ near-shore buoy data. *Ocean Engineering*, *83*, 24–35. https://doi.org/10.1016/j.oceaneng.2014.03.014

Shay, L. K., Elsberry, R. L., & Black, P. G. (1989). Vertical structure of the ocean current response to a hurricane. *Journal of Physical Oceanography*, *19*(5), 649–669. https://doi.org/10.1175/1520-0485(1989)019<0649:VSOTOC>2.0.CO;2

Shchepetkin, A. F., & McWilliams, J. C. (1998). Quasi-monotone advection schemes based on explicit locally adaptive dissipation. *Monthly Weather Review*, *126*(6), 1541–1580. https://doi.org/10.1175/1520-0493(1998)126<1541:QMASBO>2.0.CO;2

Smith, R. K., Montgomery, M. T., & Van Sang, N. (2009). Tropical cyclone spin-up revisited. *Quarterly Journal of the Royal Meteorological Society*, *135*(642), 1321–1335. https://doi.org/10.1002/qj.428

Smith, S. D. (1988). Coefficients for sea-surface wind stress, heat-flux, and wind profiles as a function of wind-speed and temperature. *Journal of Geophysical Research*, *93*(C12), 15467–15472. https://doi.org/10.1029/JC093iC12p15467

Sofiev, M., Soares, J., Prank, M., de Leeuw, G., & Kukkonen, J. (2011). A regional-to-global model of emission and transport of sea salt particles in the atmosphere. *Journal of Geophysical Research*, *116*, D21302. https://doi.org/10.1029/2010JD014713

Song, Y., & Haidvogel, D. (1994). A semi-implicit ocean circulation model using a generalized topography-following coordinate system. *Journal of Computational Physics*, *115*(1), 228–244. https://doi.org/10.1006/jcph.1994.1189

Tannehill, I. R. (1936). Sea swells in relation to movement and intensity of tropical storms. *Monthly Weather Review*, *64*(7), 231–238. https://doi.org/10.1175/1520-0493(1936)64<231b:SSIRTM>2.0.CO;2

The WAVEWATCH III Development Group (WW3DG) (2016). *User manual and system documentation of WAVEWATCH III version 5.16* (Tech. Note 329). College Park, MD: NOAA/NWS/NCEP/MMAB.

Tolman, H. L. (1992). Effects of numerics on the physics in a third-generation wind-wave model. *Journal of Physical Oceanography*, *22*(10), 1095–1111. https://doi.org/10.1175/1520-0485(1992)022<1095:EONOTP>2.0.CO;2

Tolman, H. L. (2002). Alleviating the garden sprinkler effect in wind wave models. *Ocean Modelling*, *4*(3–4), 269–289. https://doi.org/10.1016/S1463-5003(02)00004-5

Tulet, P., Crassier, V., Cousin, F., Suhre, K., & Rosset, R. (2005). ORILAM, a three-moment lognormal aerosol scheme for mesoscale atmospheric model: Online coupling into the Meso-NH-C model and validation on the Escompte campaign. *Journal of Geophysical Research*, *110*, D18201. https://doi.org/10.1029/2004JD005716

Uchiyama, Y., McWilliams, J. C., & Restrepo, J. M. (2009). Wave-current interaction in nearshore shear instability analyzed with a vortex force formalism. *Journal of Geophysical Research*, *114*, C06021. https://doi.org/10.1029/2008JC005135

Voldoire, A., Decharme, B., Pianezze, J., Lebeaupin Brossier, C., Sevault, F., Seyfried, L., et al. (2017). SURFEX v8.0 interface with OASIS3-MCT to couple atmosphere with hydrology, ocean, waves and sea-ice models, from coastal to global scales. *Geoscientific Model Development*, *10*(11), 4207–4227. https://doi.org/10.5194/gmd-10-4207-2017

Wada, A., Uehara, T., & Ishizaki, S. (2014). Typhoon-induced sea surface cooling during the 2011 and 2012 typhoon seasons: Observational evidence and numerical investigations of the sea surface cooling effect using typhoon simulations. *Progress in Earth and Planetary Science*, *1*(1), 11. https://doi.org/10.1186/2197-4284-1-11

Wada, A., Usui, N., & Sato, K. (2012). Relationship of maximum tropical cyclone intensity to sea surface temperature and tropical cyclone heat potential in the North Pacific Ocean. *Journal of Geophysical Research*, *117*, D11118. https://doi.org/10.1029/2012JD017583

Wang, X., Deane, G. B., Moore, K. A., Ryder, O. S., Stokes, M. D., Beall, C. M., et al. (2017). The role of jet and film drops in controlling the mixing state of submicron sea spray aerosol particles. *Proceedings of the National Academy of Sciences of the United States of America*, *114*(27), 6978–6983. https://doi.org/10.1073/pnas.1702420114

Wang, Y., Kepert, J. D., & Holland, G. J. (2001). The effect of sea spray evaporation on tropical cyclone boundary layer structure and intensity. *Monthly Weather Review*, *129*(10), 2481–2500. https://doi.org/10.1175/1520-0493(2001)129<2481:TEOSSE>2.0.CO;2

Warner, J. C., Armstrong, B., He, R., & Zambon, J. B. (2010). Development of a coupled ocean-atmosphere-wave-sediment transport (COAWST) modeling system. *Ocean Modelling*, *35*(3), 230–244. https://doi.org/10.1016/j.ocemod.2010.07.010

Wilson, T. W., Ladino, L. A., Alpert, P. A., Breckels, M. N., Brooks, I. M., Browse, J., et al. (2015). A marine biogenic source of atmospheric ice-nucleating particles. *Nature*, *525*(7568), 234–238.

Wright, C. W., Walsh, E. J., Vandemark, D., Krabill, W. B., Garcia, A. W., Houston, S. H., et al. (2001). Hurricane directional wave spectrum spatial variation in the open ocean. *Journal of Physical Oceanography*, *31*(8), 2472–2488. https://doi.org/10.1175/1520-0485(2001)031<2472:HDWSSV>2.0.CO;2

Zambon, J. B., He, R., & Warner, J. C. (2014). Investigation of hurricane Ivan using the coupled ocean-atmosphere-wave-sediment transport (COAWST) model. *Ocean Dynamics*, *64*(11), 1535–1554. https://doi.org/10.1007/s10236-014-0777-7

Zhang, H., Chen, D., Zhou, L., Liu, X., Ding, T., & Zhou, B. (2016). Upper ocean response to typhoon Kalmaegi (2014). *Journal of Geophysical Research: Oceans*, *121*, 6520–6535. https://doi.org/10.1002/2016JC012064

Zhao, B., Qiao, F., Cavaleri, L., Wang, G., Bertotti, L., & Liu, L. (2017). Sensitivity of typhoon modeling to surface waves and rainfall. *Journal of Geophysical Research: Oceans*, *122*, 1702–1723. https://doi.org/10.1002/2016JC012262